Quantifying Watershed Criticality via Deep Learning and Explainable AI for Groundwater Resilience

Özlem Baydaroğlu[1], Serhan Yeşilköy[2]

[1] National Academies of Sciences, Engineering, and Medicine, Washington, DC, USA

[2] Turkish Ministry of Agriculture and Forestry, İstanbul Provincial Directorate, İstanbul, Türkiye

Abstract

Groundwater is a vital freshwater resource that supports drinking water supply, agricultural sustainability, ecosystem functioning, and drought resilience. As water scarcity and climate change impacts intensify, sustainable groundwater management plays an important role in groundwater management, with groundwater storage (GWS) acting as a key indicator of groundwater resilience. This study introduces an integrated, data-driven framework combining deep learning and explainable artificial intelligence (XAI) to analyze GWS anomalies and quantify watershed criticality across Türkiye. Utilizing Empirical Orthogonal Functions (EOF) for dimensionality reduction of hydro-climatic variables, including GWS, precipitation, and evapotranspiration, a spatiotemporal prediction model based on the Graph WaveNet (GWN) architecture has been developed to capture complex spatial and temporal dependencies. To evaluate watershed-specific vulnerabilities, SHAP (SHapley Additive exPlanations) values have been leveraged to isolate the direct pressure of individual climatic drivers on GWS variations. These predictive and explanatory indicators have been subsequently fused with historical GWS-derived features to establish a multi-criteria watershed criticality score, the robustness of which has been rigorously validated through comprehensive sensitivity analyses. The proposed framework successfully identifies watersheds at imminent risk, offering a scalable projection tool to enhance watershed resilience and support proactive policymaking against climate-induced water scarcity.

Keywords: Groundwater storage, Graph WaveNet, SHAP, Watershed Criticality, Water resilience

---

---

1. Introduction

Groundwater accounts for the largest freshwater resources on Earth and becomes an integral part of the water cycle (Aeschbach-Hertig and Gleeson, 2012). Globally, groundwater resources account for around 30% of all freshwaters. Groundwater supplies more than 40% of water demand in irrigated agriculture and hence plays a crucial role in food security (Gleeson et al., 2012; Kuang et al., 2024) and 25% for potable water requirements, and the 10% for industrial applications (Ahmadi et al., 2020). Therefore, groundwater resource quantification is a critical challenge in densely populated regions to provide sufficient amounts of freshwater.

Climate change and the resulting shifts (Yeşilköy and Baydaroğlu, 2025) in the water cycle have accelerated research on groundwater resources (Yeşilköy et al., 2024). Various studies have investigated groundwater dynamics across different regions of the world. For instance, Clark et al. (2025) utilized a multilayer perceptron (MLP) neural network model coupled with XAI tools. They aimed to determine whether groundwater level declines in Australia's largest hydrological system were driven by climatic factors or human activities. Their findings revealed that the most critical drivers affecting groundwater level changes were groundwater extraction (number of wells), floods, annual precipitation, and potential evapotranspiration (hereafter "ET"). Chakraborty et al. (2021) investigated the factors influencing groundwater level fluctuations in Texas, USA, utilizing Extreme Gradient Boosting (XGBoost) and XAI. The results indicated that long-term drought indices along with cumulative precipitation deficits, were the most substantial predictors of changes in groundwater levels. Similarly, Li et al. (2024) analyzed groundwater storage dynamics in Shandong Province, China, to examine their driving factors and develop short-term forecasting models. Their findings demonstrated that combining satellite-based data with hydrological models provides highly accurate results for regional groundwater monitoring. Furthermore, they revealed that Support Vector Machine (SVM)-based AI models can be reliably used for short-term water management planning. Adam et al. (2026) combined GRACE satellite data with the Random Forest (RF) method and Global Land Data Assimilation System (GLDAS) surface hydrological models to track groundwater storage dynamics. Raju et al. (2024) tested multiple linear regression and machine learning (ML) algorithms to predict GWS in the Indo-Gangetic Plains of India, using hydroclimatic inputs such as precipitation, ET, soil moisture, and runoff. Among the tested methods, the RF algorithm showed the most stable performance in capturing complex hydroclimatic relationships.

Approximately 18% of Türkiye's total water resource potential comprises groundwater resources. A substantial portion of the flow in major rivers is derived from groundwater via springs and baseflow. The groundwater resources of Türkiye are predominantly situated within alluvial and karst aquifers (Yazicigil and Ekmekci, 2019). Groundwater studies in Türkiye has primarily focused on groundwater characteristics, pollution, including the assessment of arsenic levels (Gunduz et al., 2010), nitrate contamination (Nas and Berktay, 2006; Yesilnacar et al., 2008; Güler et al., 2012), and zinc concentrations (Güler et al., 2012; Kara, 2025) and their associated health impacts (Baba and Tayfur, 2011; Davraz and Batur, 2021). Moreover, several studies have evaluated general groundwater quality indicators (Taşan, 2025, Tayfur et al., 2008; Tokatli et al.,

2013; Kavurmaci and Üstün, 2016; Yetiş et al., 2019; Taşan, 2025) and salinization processes (Güler et al., 2012). Aksoy et al. (2009) investigated the Balçova Geothermal Field in İzmir and reported that the intrusion of toxic elements, such as arsenic, antimony, and boron, into shallow aquifers restricted the use of these waters for household consumption and agricultural irrigation. In a study focusing on Türkiye's 25 watersheds, Dilcan and Koksal (2026) modeled the interactions between water resources, energy production, and climate change for the 2023–2053 period to quantify the freshwater consumption of hydroelectric and fossil-fueled power plants. Furthermore, the Kızılırmak, Euphrates–Tigris, Gediz, Ceyhan, and Sakarya watersheds were identified as areas facing the highest water stress, whereas the Eastern Black Sea, Aras, and Eastern Mediterranean watersheds were classified as more water-secure regions. Several studies have also focused on forecasting groundwater levels and potential at different scales in different part of Türkiye through various methodologies like multiple linear regression (MLR), ANFIS, radial basis neural network (RBNN), and SVM (Demirci et al., 2019), analytical hierarchy process (AHP) and frequency ratio (FR) (Ahmadi et al., 2020), binary logistic regression (Ozdemir, 2011), multi-criteria and heuristic methods (Bozdağ et al., 2025). Ertürk et al. (2014) investigated the impacts of climate change on groundwater resources in the Köyceğiz-Dalyan special environmental protection area within the eastern Mediterranean watershed using the Soil and Water Assessment Tool (SWAT) model. Their simulation results indicated a clear decline in both groundwater recharge and storage. Karatas et al. (2026) evaluated the spatiotemporal variations in groundwater depth (GD) and salinity (e.g., EC) across the southern part of Türkiye. Their findings revealed that the slope of the GD trend increased across nearly the entire area, whereas the slope of the EC trend increased in only 16% of the study region.

This study analyzes the spatiotemporal variations of groundwater storage across Türkiye to identify the most critical watersheds using a multi-criteria approach. The main objective is to provide a projection tool for watersheds exhibiting high vulnerability and an increased probability of encountering future water scarcity.

Our framework consists of five main analytical steps. First, Empirical Orthogonal Functions (EOFs) are applied to GWS, precipitation, and evapotranspiration data for each watershed to achieve dimensionality reduction through principal components. Second, a spatiotemporal prediction model is constructed using GWN architecture. Third, watershed-specific SHAP values are computed to quantify the impact of individual hydro-climatic variables within the prediction model. Fourth, a watershed criticality score is established for each watershed by fusing historical GWS-derived features with the predictive and explanatory indicators, where relative weights are assigned to each feature. Finally, the robustness of the calculated criticality scores is validated through a comprehensive sensitivity analysis.

2. Materials and Methods

2.1 Study Area

There are twenty-five watersheds (Fig. 1, Latitude: 36-42°N, Longitude: 26-45°E) and important water resource management projects (i.e., the Southeastern Anatolia Project (Güneydoğu Anadolu

Projesi (GAP) in Turkish), and hydropower plant facilities across Türkiye. According to the Turkish Statistical Institute (TURKSTAT, 2024; https://veriportali.tuik.gov.tr/en/press/ 53699), the population number is 86.1 million and expected to increase to 94 million by 2050. In addition to population growth, climate change will exacerbate the pressure on water resources due to precipitation instability and increased evaporation from surfaces.

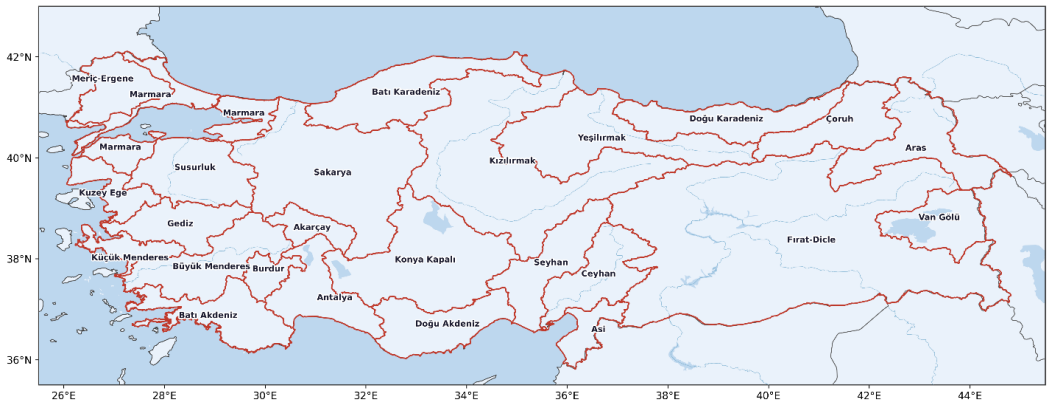

Figure 1. Türkiye's watersheds. Red lines represent the borders of watersheds, and their names are in the center.

2.2 Data

Daily gridded GWS has been downloaded from the National Aeronautics and Space Administration's (NASA) Global Land Data Assimilation System (GLDAS) data (version 2.2) with 0.25° spatial resolution from October 1st, 2004, to September 30th, 2024, through the NASA Goddard Earth Sciences Data and Information Services Center (GES DISC). (Li et al., 2020). Gridded daily ET and hourly precipitation data in the same period have been obtained through the ECMWF's AgERA5 and ERA5-land hourly databases with 0.1° spatial resolution, respectively. Hourly precipitation and daily ET data have been converted to monthly total and daily GWS has been converted to monthly mean because of being a stock variable (Djessou et al., 2022) representing the state of the aquifer at a specific point in time, temporal aggregation has been performed by calculating the arithmetic mean rather than the cumulative sum. This approach ensures physical consistency, as GWS reflects an instantaneous volume, whereas flow variables such as precipitation or evapotranspiration are summed over the respective period. To provide spatial resolution consistency, GWS data have been regridded to 0.1-degree to provide spatial resolution consistency. All data have been partitioned using water years (WY, the total number of WY is 21) from October to September rather than calendar years to preserve seasonal integrity at training/test boundaries.

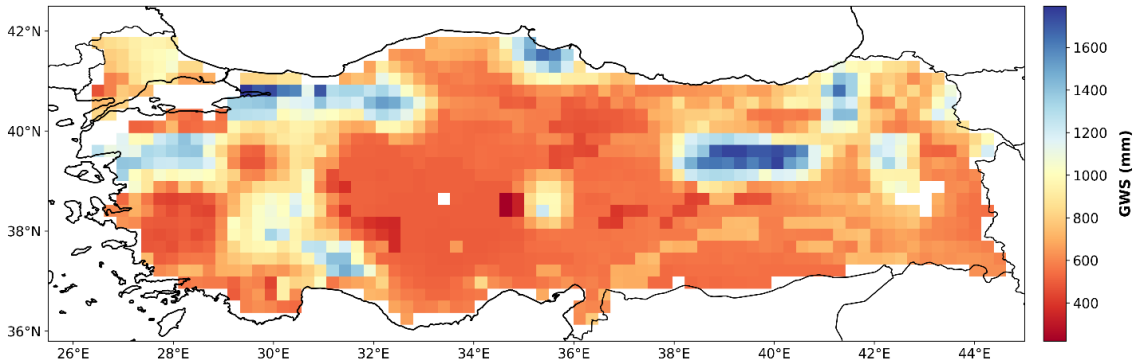

Figure 2. Spatial distribution of GWS in Türkiye between the years 2023 and 2024 (21 water years).

The number of populations at district-level has been obtained through the TURKSTAT and there is a discrepancy between the watershed and the district boundaries. To address this, the areas of the districts located within the watershed boundaries have been calculated, and population figures have been separated according to the area covered by each watershed. This step has been performed with open-access QGIS software (version 3.40) The population density of each watershed can be found in Fig. 3.

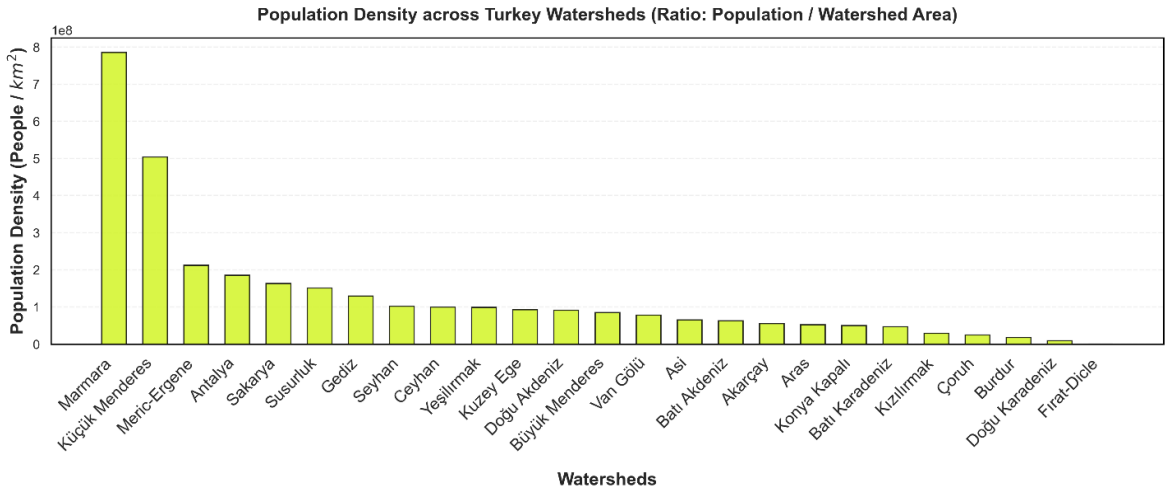

Figure 3. Population density (Population/Watershed Area) across Türkiye watersheds.

2.2.1 Data Normalization

Three distinct normalization procedures have been applied sequentially to ensure methodological consistency and prevent data leakage across training and test periods (Davari et al., 2025). First, EOF input fields have been mean-centered via temporal mean subtraction (anomaly decomposition) following the examples of Conlin et al. (2020) and Fraehr et al. (2022). Subtracting the temporal mean isolates the anomaly field, the departure from the long-term climatological state, which is the quantity of hydrological interest. Consequently, all EOF principal component scores, and by extension all model predictions, represent GWS anomalies relative to the long-term climatological mean rather than absolute storage values.

Second, the node feature matrix X has been standardized using z-score normalization ($X_{scaled}=\frac{X-\mu_{train}}{\sigma_{train}}$), where μ_{train} and σ_{train} denote the mean and standard deviation computed exclusively over the training period and subsequently applied to both training and test sets. This step is essential because the input features span heterogeneous physical units and magnitude ranges, GWS is expressed in mm, population density in persons/km², and trend slope in mm/month, and without normalization, features with large absolute values would dominate gradient updates during backpropagation, destabilizing training and biasing learned representations toward high-magnitude inputs.

Third, the target variable Y (GWS EOF Mode 1 at forecast horizon $t+h$) has also been z-score normalized using training-period statistics prior to model optimization. Following inference, predictions have been back-transformed to physical units via $\hat{y}_{\text{mm}}=\hat{y}_{\text{scaled}}\cdot\sigma_{train}+\mu_{train}$. Normalizing the target ensures that the Huber loss function operates on a dimensionless, unit-variance quantity, providing numerically stable gradients regardless of the absolute magnitude of GWS variability across watersheds. The inverse transformation restores interpretable units (mm) for subsequent analysis and visualization.

In all three cases, normalization parameters have been estimated solely from training data and applied to the test set without re-estimation, ensuring strict temporal separation between training and evaluation phases and eliminating any possibility of data leakage.

2.3. Methods

The objective of this study is to assess Türkiye's groundwater potential and identify watersheds vulnerable to climate change and anthropogenic pressures (e.g., unsustainable water management, migration), ultimately providing future estimates. To achieve this, a predictive framework has been developed using EOF (Lorenz, 1956) decomposition and GWN (Wu et al., 2019). Furthermore, XAI has been utilized to analyze the driving factors influencing GWS. A multi-component criticality score has been established to identify the most vulnerable watersheds. To validate both the criticality scores and the selection of the most critical watersheds, a sensitivity analysis has been conducted using the One-At-a-Time (OAT) (Morris, 1991) and Monte Carlo (MC) (Helton, 1993) simulations.

2.3.1 Empirical Orthogonal Function (EOF)

During the data pre-processing stage, different approaches and testing methods (Baydaroğlu et al., 2024) have been evaluated to identify the most suitable representation of the data for achieving high predictive performance (Baydaroğlu et al., 2025). For the watershed-scale analysis, spatial averaging has not been adopted because the study watersheds differ considerably in size, which may lead to the loss of important spatial information. Grid-based representation has also been considered; however, treating each grid independently may result in strong redundancy among neighboring grids within the same watershed and may limit the model's ability to learn watershed-scale dynamics.

Therefore, EOF has been employed in the pre-processing stage. EOF provides physically interpretable spatial modes together with corresponding time series for each mode, allowing an efficient representation of the dominant variability patterns while generating suitable inputs for the prediction model.

EOF is a function that enables the decomposition of a continuous space-time field $X(t,s)$, where t and s represent time and spatial position, respectively. $X(t,s)=\sum_{k=1}^{M} c_k(t)u_k(s)$ where M denotes the number of modes present in the field, utilizing an optimal set of spatial basis functions $u_k(s)$ and temporal expansion functions $c_k(t)$ (Hannachi et al., 2007).

EOF analysis has been applied separately to the groundwater storage (GWS), precipitation, and ET data for each watershed. The decomposition has been performed using Singular Value Decomposition (SVD). Figure 4 shows the mode-wise explained variance averaged across all watersheds, together with the corresponding standard deviations (mean ± standard deviation). The dominance of Mode 1 is the most pronounced in ET, followed by GWS and precipitation, with subsequent modes contributing minimally to the total variance.

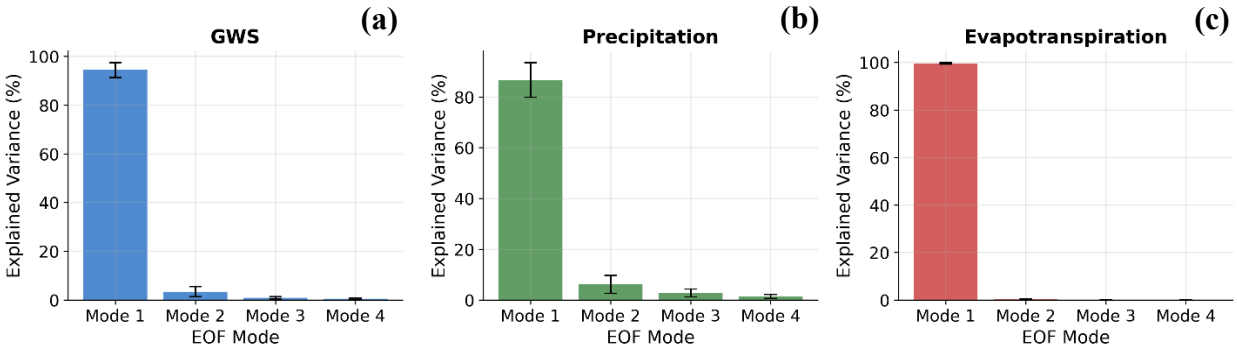

Figure 4. Explained variance by EOF modes for (a) GWS, (b) precipitation, and (c) evapotranspiration. Values indicate the mean ± standard deviation across 25 watersheds.

Following similar approaches in the literature (Wang et al., 2015; Ham et al., 2019), to reduce input dimensionality, the features for the GWS, precipitation, and ET groups have been represented by GWS EOF1–4, Prec EOF1–4, and ET EOF1–4, respectively.

The data pipeline of the model is described below. This process converts high-dimensional pixel-based data into low-dimensional summaries (EOFs). Then, a hybrid deep learning model analyzes both spatial and temporal dependencies.

i) The starting point is high-dimensional raw pixel data ($T \times P_i$), which shows how many pixels (P) in each watershed (i) change over time (T).

ii) EOF analysis has been performed for each watershed using Singular Value Decomposition (SVD). This step produces principal component scores ($T \times K_i$) that represent the variance of thousands of grids. This reduces the data size, filters out noise, and makes calculations more efficient.

iii) This node feature tensor is used as input for the GWN model. The model simultaneously processes both historical time-series data and the spatial relationships between watersheds.

Additionally, EOF spatial patterns have been estimated exclusively using the training period. To prevent temporal data leakage, test-period PC scores have been obtained by projecting test data onto these pre-computed training EOF patterns. Input features used in the GWN model and GradientSHAP analysis are detailed in Table 1.

Table 1. Input features used in the GWN model and GradientSHAP analysis.

Group	Feature	Type	Description
GWS	EOF Mode 1-4	Dynamic	Principal component scores of GWS anomaly field (monthly mean)
Precipitation	EOF Mode 1-4	Dynamic	Principal component scores of monthly total precipitation
ET	EOF Mode 1-4	Dynamic	Principal component scores of monthly total ET
Watershed Characteristics	Long-term mean	Static	Mean GWS anomaly over training period (mm); lower values indicate chronic water stress
	Standard deviation	Static	Absolute GWS variability (mm)
	Coefficient of variation	Static	Relative variability ($std/\|mean\|$); indicator of system instability
	Minimum GWS	Static	Historical minimum GWS anomaly (mm); proxy for drought vulnerability
	Trend slope	Static	Sen's slope (mm/month); trend significance assessed via Mann-Kendall test ($p < 0.05$); long-term depletion rate
	Trend acceleration	Static	Difference between last 5-year slope and long-term slope (mm/month); detects accelerating depletion
	Seasonal amplitude	Static	Peak-to-trough range of Seasonal and Trend decomposition using Loess (STL) (Shamsudduha et al., 2009) seasonal component (mm); recharge seasonality
	Population density	Static	People/km2; proxy for anthropogenic water demand pressure
	Watershed area	Static	km^2; spatial scale of the hydrological unit

Dynamic features vary at each timestep; static features are time-invariant node attributes broadcast across all time steps. EOF modes have been computed separately for each watershed using training-period data only (N=4 modes per variable). All features have been z-score normalized using training-period statistics prior to model input.

In addition, the GWS EOF1 anomaly is defined as the target variable, representing the millimeter-scale deviation of groundwater storage (GWS) from its long-term average. The objective is to predict this anomaly with a 60-month (5-year) lead time. A 3-month rolling mean has been employed to smooth the GWS time series, thereby mitigating high-frequency noise and enhancing the visibility of underlying trends (Ghosh et al., 2026; Chihana et al., 2026).

2.3.2 Graph WaveNet (GWN)

GWS exhibits strong spatiotemporal dependencies: adjacent watersheds may share similar precipitation regimes, recharge dynamics, and in some cases hydraulic connectivity, making the prediction of GWS in one watershed partially dependent on the hydrometeorological state of its neighbors. To exploit these dependencies, this study employs GWN (Wu et al., 2019), a deep learning architecture that combines graph-based spatial convolution with dilated causal temporal convolution within a single framework.

The spatial structure of the problem is encoded as a directed graph $G=(V, E, A)$ where V is the set of nodes, E is the set of edges, and edge weights are defined by a hybrid adjacency matrix: $A=\alpha A_{geo}+(1-\alpha)A_{corr}$, where A_{geo} encodes geographic contiguity (binary indicator of shared watershed boundaries) and A_{corr} encodes pairwise Pearson correlations between GWS EOF Mode1 time series computed during the training period, thresholded at $r>0.3$ to retain only statistically meaningful connections. Equal weighting ($\alpha=0.5$) has been applied to balance physical proximity and hydrological similarity. Both matrices have row-normalized prior to combination.

A key feature of GWN is the inclusion of a self-adaptive adjacency matrix $\tilde{A}_{adp}$, learned end-to-end during training: $\tilde{A}_{adp}=softmax(ReLU(E_1E_2^T))$, where $E_1, E_2 \in R^{N\times d}$ are trainable node embedding matrices. This component allows the model to capture latent spatial dependencies not encoded in the predefined adjacency structure. The final adjacency used in each graph convolution layer is $A_{final}=0.5\ A+\ 0.5\ \tilde{A}_{adp}$

Figure 5 shows graph Adjacency matrix based on geographic contiguity and GWS correlation.

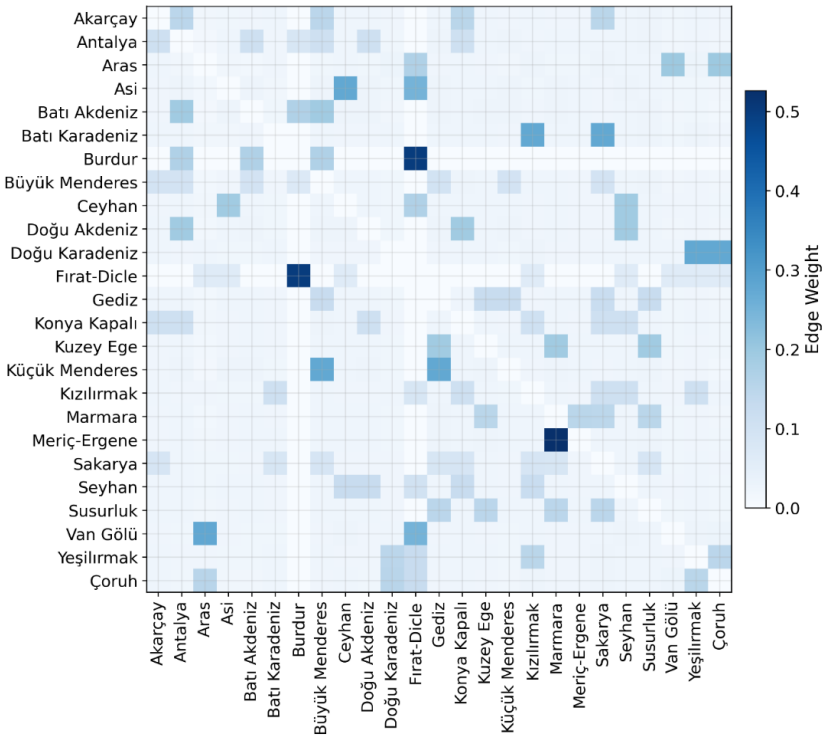

Figure 5. Graph Adjacency matrix based on geographic contiguity and GWS correlation.

Temporal dependencies are captured through stacked dilated causal convolution layers with exponentially increasing dilation factors d=1,2,4,8. The progressively increasing dilation factors allow the model to capture temporal dependencies over multiple time scales by expanding the receptive field in successive layers. In this framework, the first layer primarily captures short-term variations (1–3 months), while subsequent layers extract medium-term (2–6 months), seasonal (4–12 months), and longer-term (8–24 months) temporal patterns. This multi-scale design, adopted from the WaveNet architecture, enables efficient modeling of both local and long-range temporal dynamics without a substantial increase in computational complexity. Gated activations of the form: $z=tanh(W_f{}^{*}x) \odot \sigma(W_g{}^{*}x)$, where * denotes convolution element-wise multiplication, regulating information flow through the network analogously to the gating mechanism in LSTM architectures, but with greater computational efficiency and explicit multi-scale temporal receptive fields. Here, x denotes the input hidden-state tensor from the previous layer, W_f and W_g are the convolutional weights of the filter and gate branches, respectively, $tanh(\cdot)$ is the filter activation function, $\sigma(\cdot)$ sigmoid gate activation function, and z (output) is the resulting gated output passed to the subsequent layer.

The model receives as input the node feature tensor $X \in R^{T_{seq} \times N \times F}$, where T_{seq}=120 months (input window), N=25 watersheds, and F=21 features per node (12 dynamic EOF modes + 9 static watershed characteristics), and produces a single forecast $\hat{y}_{t+h} \in R^N$ for horizon $h \in \{12, 24, 36, 48, 60\}$ months. Model parameters have been optimized using the Adam optimizer (Zhang, 2018; Baydaroğlu and Demir, 2024) (learning rate 3×10^{-4}, weight decay 5×10^{-4}) with a Huber loss function (δ=1.0) and cosine annealing warm restart scheduling. Training has been performed on a strict temporal holdout: the first 16 water years October 2003 – September 2019) constituted the training set and the final 5 water years (October 2019 - September 2024) the independent test set.

The GWN model predicts the normalized EOF1 anomaly of GWS for a given prediction horizon. The predicted EOF1 values are then converted back to GWS anomalies using inverse scaling. This integrated framework effectively captures both temporal dynamics and spatial dependencies in groundwater systems while reducing the dimension of the original gridded dataset. Consequently, the dominant spatiotemporal variability is retained, enabling more accurate predictions. The hyperparameters adopted for the GWN model are listed in Table 2.

Table 2. Hyperparameters used in the GWN model

Parameter	Value	Explanation
N_EOF	4	Number of EOF modes per variable
SEQ_LEN	120 months	Input sequence length (=2×forecast horizon)
FORECAST_HORIZON	60 months	Forecast horizon (5 years)
GWN_HIDDEN	32	Hidden layer dimensionality
GWN_LAYERS	4	Number of WaveNet layers (dilation=1,2,4,8)
GWN_DROPOUT	0.4	Dropout rate for regularization
BATCH_SIZE	8	Mini-batch size
N_EPOCHS	150	Maximum training epochs

Learning rate	$3x10^{-4}$	Adam optimizer initial learning rate
Weight decay	$5x10^{-4}$	L2 regularization coefficient
PATIENCE	30	Early stopping patience
Correlation threshold	0.3	Minimum Pearson r for adjacency matrix edge inclusion
Huber loss	1.0	Transition point between L2 and L1 loss regions
Scheduler	CosineAnnealingWarmRestarts	T_0=30, T_{mult}=2, η_{min}=10^{-5}
Optimizer	Adam	β_1=0.9, β_2=0.999 (PyTorch defaults)

All hyperparameters have been set prior to training and held constant across all watersheds and all forecast horizons (h = 12, 24, 36, 48, 60 months).

2.3.3 Explainability and Criticality

Traditional approaches that rely exclusively on groundwater trends may categorize watersheds with analogous diminishing storage patterns into the same risk classification. The suggested SHAP-based Criticality Score system elucidates the fundamental causes and resilience of each watershed. A watershed exhibiting a continual decrease in GWS and a feeble seasonal recharge signal may be intrinsically more susceptible than a watershed with a similar dropping trend but a robust seasonal cycle. The methodology integrates predictive, explanatory, and historical groundwater indicators to identify watersheds with diminished recovery potential and increased criticality, thus facilitating better informed groundwater management decisions.

Following the feature engineering and XAI paradigm commonly used in the literature, feature attribution has been performed using GradientSHAP (Captum library), an implementation of the SHAP framework adapted for gradient-based deep learning models for SHAP analysis and watershed criticality assessment. These features included the long-term GWS trend (Mann–Kendall), GWS trend acceleration (recent 5-year trend minus long-term trend), mean GWS, GWS variability (coefficient of variation), minimum GWS, GWS seasonal amplitude, and population densities of watersheds. These features have been subsequently integrated into the criticality assessment framework to provide a comprehensive evaluation of watershed conditions and resilience.

The workflow of this research stage proceeds as follows: First, to understand the driving factors behind the predictions, SHAP values have been determined individually for each watershed using the GWS anomaly prediction model. This watershed-specific approach has been adopted because each watershed exhibits distinct environmental and hydrogeological characteristics, allowing the model to quantify the exact contribution and influence of each input variable per watershed. Subsequently, a criticality score has been established for each watershed by utilizing the derived features, the model predictions, and the calculated SHAP values as independent features, where a specific weight is assigned to each feature component. To validate the reliability and accuracy of the computed criticality scores, a comprehensive sensitivity analysis is conducted. This analysis employs the widely-used OAT (Singh et al., 2022; Owais and Ramadan, 2025; Li et al., 2026) alongside the MC methods (Ge and Asgarpoor, 2011; Campelo et al., 2016). Through

this dual sensitivity assessment, the robustness of the feature weight selection and the stability of the final watershed rankings are rigorously verified.

2.3.3.1 Explainability

Unlike traditional AI methods that operate as black-box systems, XAI approaches, such as SHAP analysis, have been developed to improve transparency and interpretability by quantifying the contribution of specific variables to model predictions (Demiray et al., 2025). SHAP is a widely utilized XAI method grounded in cooperative game theory. It aims to explain predictive models by treating every feature (or predictor) as a player and the model outcome as the payout (Lundberg and Lee, 2017; Salih et al., 2025). A primary strength of SHAP is its capacity to quantify both the magnitude and direction of a feature's influence on a specific prediction, thereby facilitating both global and local interpretability (Lundberg et al., 2020; Mermer et al., 2026).

In this study, in addition to GWS, P, and ET variables for SHAP analysis, watershed characteristics have also been included in the analysis (see Table 1). The coefficient of variation and seasonal amplitude have been selected to characterize both the short-term and long-term vulnerability of the watersheds. In addition to the GWS trend, GWS trend acceleration has been included as a complementary feature. This inclusion is critical for distinguishing between watersheds that exhibit identical trend magnitudes but different temporal dynamics. For instance, two watersheds may both show a long-term trend of -3 mm/year; however, one might be decelerating to -1 mm/year over the last five years, while the other is accelerating to -8 mm/year. While their average trends appear identical, their levels of criticality differ significantly. Incorporating acceleration allows the model to capture this vital distinction.

2.3.3.2 Criticality

Despite Türkiye's rich groundwater potential, the combined impacts of climate change and anthropogenic mismanagement require a detailed assessment of GWS depletion risks. This phase of the study focuses on identifying watersheds in a critical condition through a multi-dimensional criticality score. Table 3 presents the specific features and weighting factors used to determine this score.

Table 3. Features and their corresponding weights utilized in calculating the criticality score.

Feature	Weights (%)
Prediction	20
SHAP	15
GWS trend	15
GWS trend acceleration	10
GWS mean	10
GWS variability	10
GWS minimum	5
Seasonal amplitude	5
Population density	10

In the determination of the criticality score, both the model predictions and their corresponding SHAP values have been treated as distinct features. The prediction represents the model's estimate of GWS conditions with a 5-year lead time. In essence, it serves as a synthesis of all learned information, including temporal patterns, cross-watershed relationships, and feature interactions, providing a direct answer to whether a watershed will experience depletion. SHAP values, on the other hand, measure the contribution and significance of each feature to the model's output. A high SHAP value indicates that the model has captured a strong, consistent signal for a specific watershed, which can be interpreted as an indicator of predictive confidence. To illustrate, two watersheds may yield identical prediction values; however, the first may exhibit low SHAP values (suggesting higher uncertainty or noise), while the second shows high SHAP values (indicating a clear and robust signal). In this context, the second watershed can be considered to be in a more critical state, as the high SHAP values suggest that the 'alarm' raised by the model is grounded in a strong evidentiary signal.

To systematically evaluate watershed vulnerability, the [0,1] normalized composite index has been classified into distinct risk regimes reflecting different levels of groundwater depletion. Values below 0.20 indicate a low-risk status, representing baseline conditions with minor storage anomalies. The range between 0.20 and 0.50 defines the moderate-risk (medium) phase, where early signs of groundwater stress begin to emerge but remain within manageable bounds. A threshold of 0.50 has been adopted as the critical inflection point delineating high-criticality watersheds; values exceeding 0.50 signify a transitional shift from moderate variations into the high and extreme risk regimes, isolating watersheds subjected to severe and urgent hydrological deficits. In Figure 6, flowchart of the integrated GWS prediction, explainability, and criticality scoring framework can be seen.

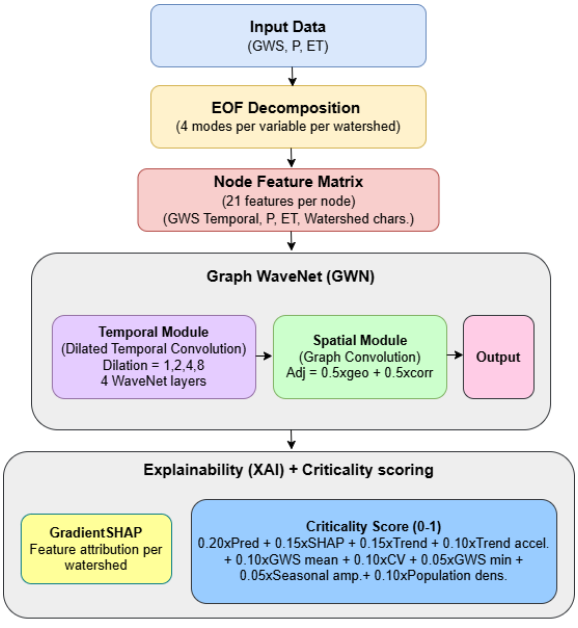

Figure 6. Flowchart of the integrated GWS prediction, explainability, and criticality scoring framework.

2.3.4 Sensitivity Analysis

While the integration of SHAP values and model predictions provides a robust framework for identifying critical watersheds, the resulting criticality scores are inherently dependent on the assigned feature weights and thus require rigorous validation. To evaluate the stability of these rankings and assess the impact of weight uncertainty, a two-stage sensitivity analysis has been conducted using OAT and MC simulations. The primary objective of this analysis is to determine the reliability of the established prioritization; specifically, it addresses whether the identified critical watersheds remain consistent under varying weighting scenarios. By quantifying the robustness of the scores, we aim to verify that the final criticality assessment is not a product of subjective weight selection but represents a stable hydrological signal.

2.3.4.1 One-at-a-time (OAT)

The partial derivatives are calculated by varying each factor separately, beginning with a base case for OAT sensitivity (Di Lullo et al., 2020). In this study, OAT analysis varied each component weight from 0% to 200% of its baseline value while rescaling the remaining weights proportionally, measuring the mean absolute rank change across all watersheds.

2.3.4.2 Monte Carlo (MC)

MC simulation is a statistical approach that uses systematic sampling of random variables to produce several random simulations of a defined scenario (Castillo et al., 2022). For the sensitivity analysis, an MC simulation (n=10000 iterations) sampled weight vectors from a Dirichlet distribution with concentration parameters proportional to the baseline weights ($\alpha = w_{baseline} \times 10$), yielding perturbed but realistic weight combinations. For each iteration, the full criticality score has been recomputed, and watershed ranks have been recorded. Rank stability has been quantified as the probability of each watershed retaining its baseline rank-1 designation.

The methodology has been implemented in Python, leveraging PyTorch for GWN construction, Captum and SHAP for interpretability, scipy.linalg.svd for EOF analysis, and pymannkendall for Mann-Kendall trend testing.

2.3.5 Performance Criteria

This study employs four fundamental metrics to evaluate the accuracy of the GWS prediction model: The Nash-Sutcliffe Efficiency (NSE) $NSE=1-\frac{\sum(X-Y)^2}{(X-\underline{X})^2}$, Root Mean Square Error (RMSE) $RMSE=\sqrt{\frac{(Y-X)^2}{n}}$, Mean absolute Percentage Error (MAPE) $MAPE(\%)=\frac{1}{n}\sum\left|\frac{X-Y}{X}\right|\times 100$, and Weighted Mean Absolute Percentage Error (wMAPE) $wMAPE(\%)=\sum\left|\frac{X-Y}{X}\right|\times 100$, where X is shows observations, Y indicates predictions, and n shows the number of considered points.

3. Results and Discussion

3.1. GWS Spatial Analysis

Türkiye GWS hotspot analysis can be seen in Figure 7. It shows the spatial distribution of GWS trends throughout Türkiye from 2003 to 2024. Negative GWS trends (red shades), indicating a decline in GWS, are predominantly observed in eastern Türkiye, the eastern, western, and the southeastern parts of the study area. In contrast, positive trends (blue shades), representing increasing GWS, are mainly concentrated in the central and western Black Sea Region ("Batı Karadeniz" in Turkish), with smaller localized areas also exhibiting increasing trends.

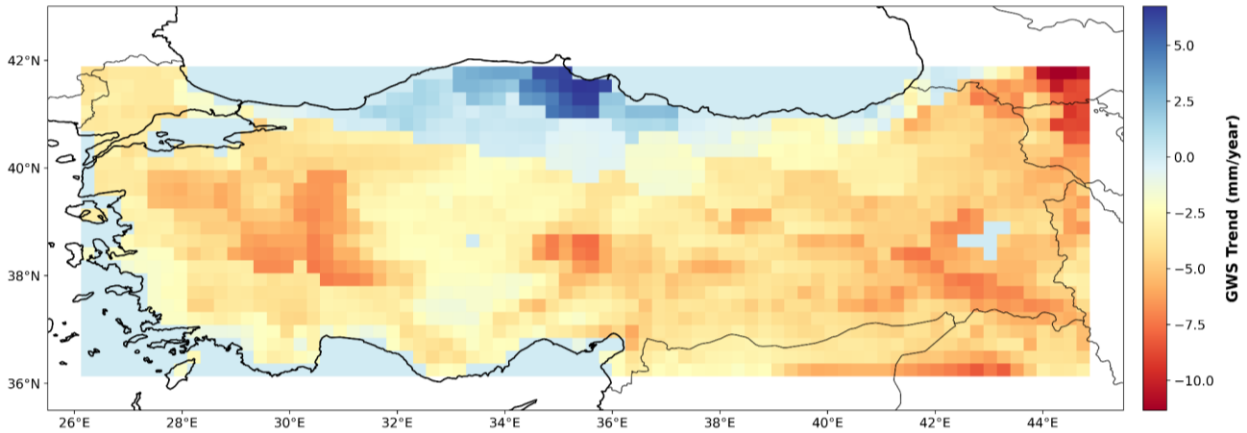

Figure 7. Spatial distribution of GWS trends (hotspot analysis) in Türkiye between the years 2003 and 2024.

3.1.1 Spatial analysis based on 10-year periods' seasons

Figure 8 compares the seasonal average spatial distribution of GWS between Period I (2004–2014 WYs) and Period II (2015–2024 WYs). Overall, the spatial distribution of GWS remains broadly consistent across the two periods. Nevertheless, Period II exhibits a noticeable expansion of low-GWS areas (red shades) in several regions, particularly across the central, the southeastern, and the western parts of Türkiye. In contrast, relatively high GWS trend values (blue shades) remain concentrated mainly along the northern coast of Türkiye. Seasonal differences are evident (Fig. 8), with summer and autumn displaying the most extensive low-GWS conditions, whereas winter and spring show relatively higher GWS due to seasonal recharge. These results suggest that although the overall spatial pattern is preserved, groundwater availability has generally declined during the more recent decade.

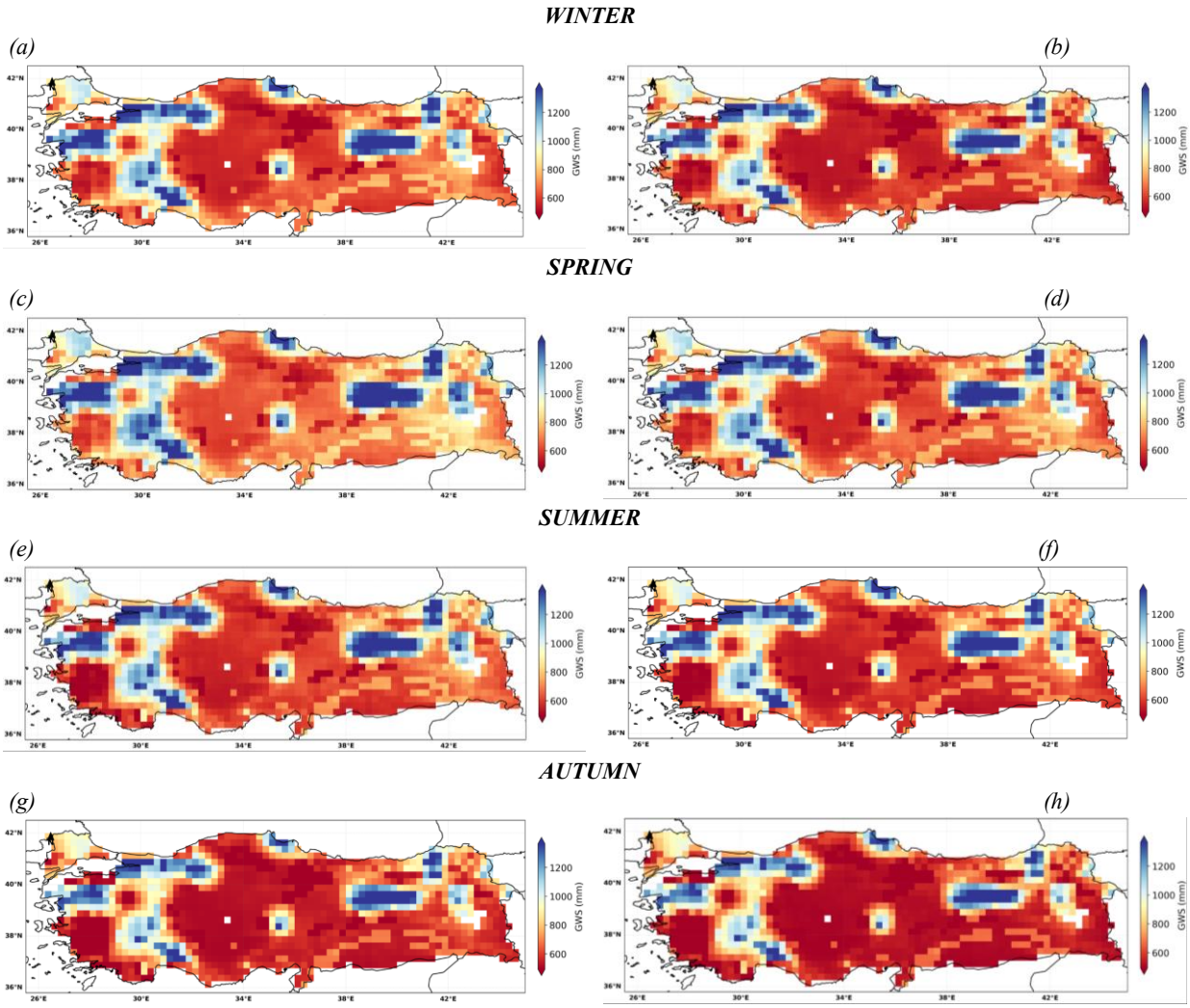

Figure 8. Mean spatial distribution of GWS in winter of (a) Period I, (b) Period II; in spring of (c) Period I, (d) Period II; in summer of (e) Period I, (f) Period II; in autumn of (g) Period I, (h) Period II.

3.1.2 Spatial detrended analysis based on 10-year periods' seasons

Figure 9 presents the seasonal average detrended GWS for Period I and Period II. Following the removal of the long-term trend, the remaining patterns primarily reflect seasonal groundwater variability. Overall, the spatial distribution of detrended GWS remains consistent between the two periods, indicating that the seasonal recharge–discharge cycle is largely preserved across Türkiye. Positive GWSs are predominantly observed during winter and spring, reflecting enhanced groundwater recharge associated with increased precipitation and snowmelt, and reduced ET. In contrast, summer and particularly autumn are characterized by widespread negative GWSs, indicating seasonal groundwater depletion driven by increased ET and water demand. Compared with Period I, Period II exhibits slightly more extensive and pronounced negative GWS values during the dry seasons, suggesting an intensification of seasonal groundwater deficits despite the removal of the long-term trend.

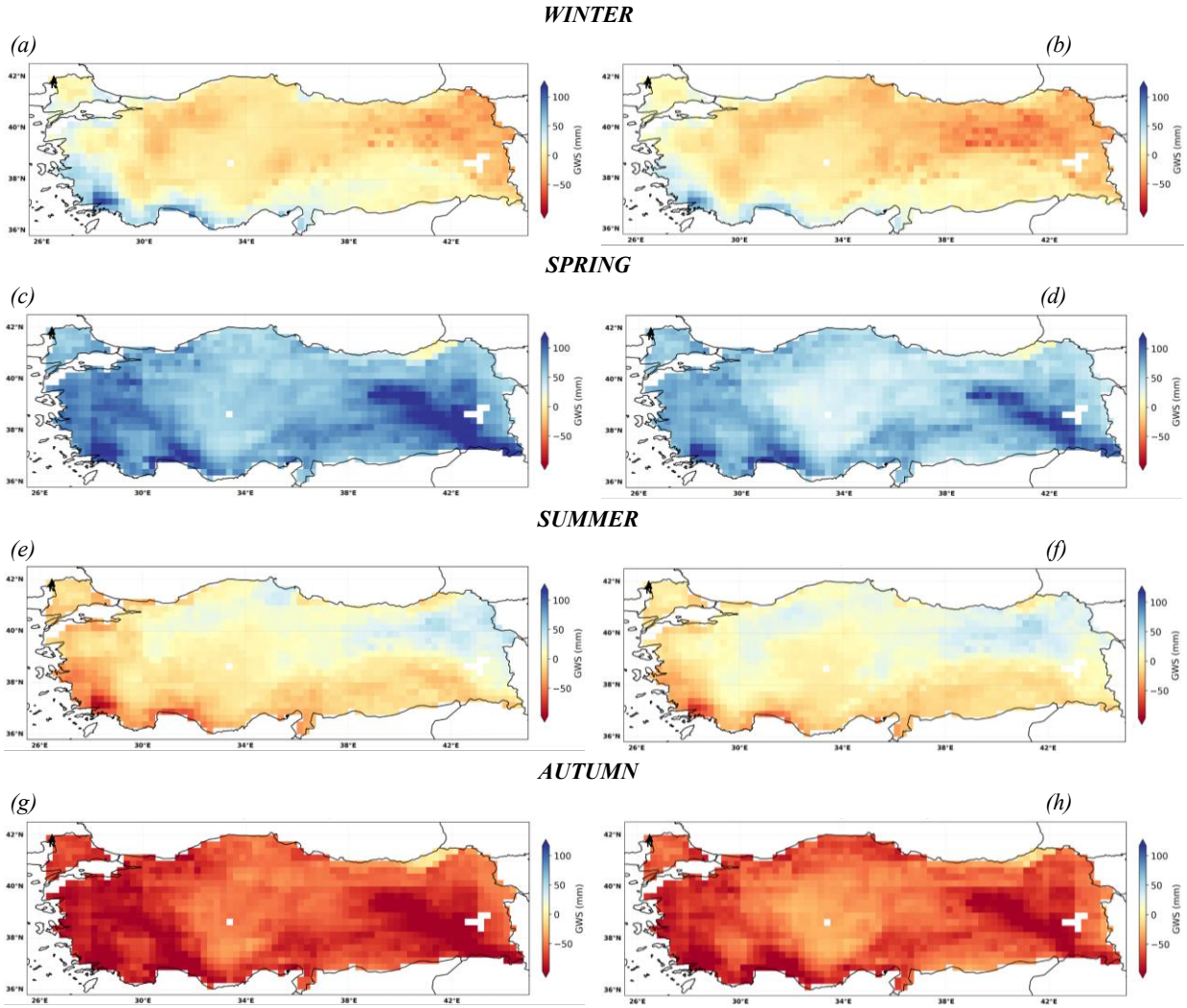

Figure 9. Mean spatial detrended distribution of GWS in winter of (a) Period I, (b) Period II; in spring of (c) Period I, (d) Period II; in summer of (e) Period I, (f) Period II; in autumn of (g) Period I, (h) Period II.

3.1.3 Spatial anomaly analysis based on 10-year periods' seasons

Figure 10 compares the seasonal GWS anomaly distributions between Period I and Period II. A clear shift in anomaly patterns is observed across all seasons. During Period I, positive GWS anomalies dominate much of Türkiye, indicating GWS conditions above the long-term seasonal average. In contrast, Period II is characterized by predominantly negative anomalies, particularly across the central, the eastern, and the southeastern parts of Türkiye, suggesting GWS below the seasonal climatology. Although localized positive anomalies remain in parts of the northern and northeastern regions, the widespread transition from positive to negative anomalies indicates a substantial deterioration in groundwater conditions during the more recent decade. This shift is evident throughout the year and is particularly pronounced during winter and spring, implying that

reduced GWS is no longer limited to the dry season but has become a persistent feature across multiple seasons.

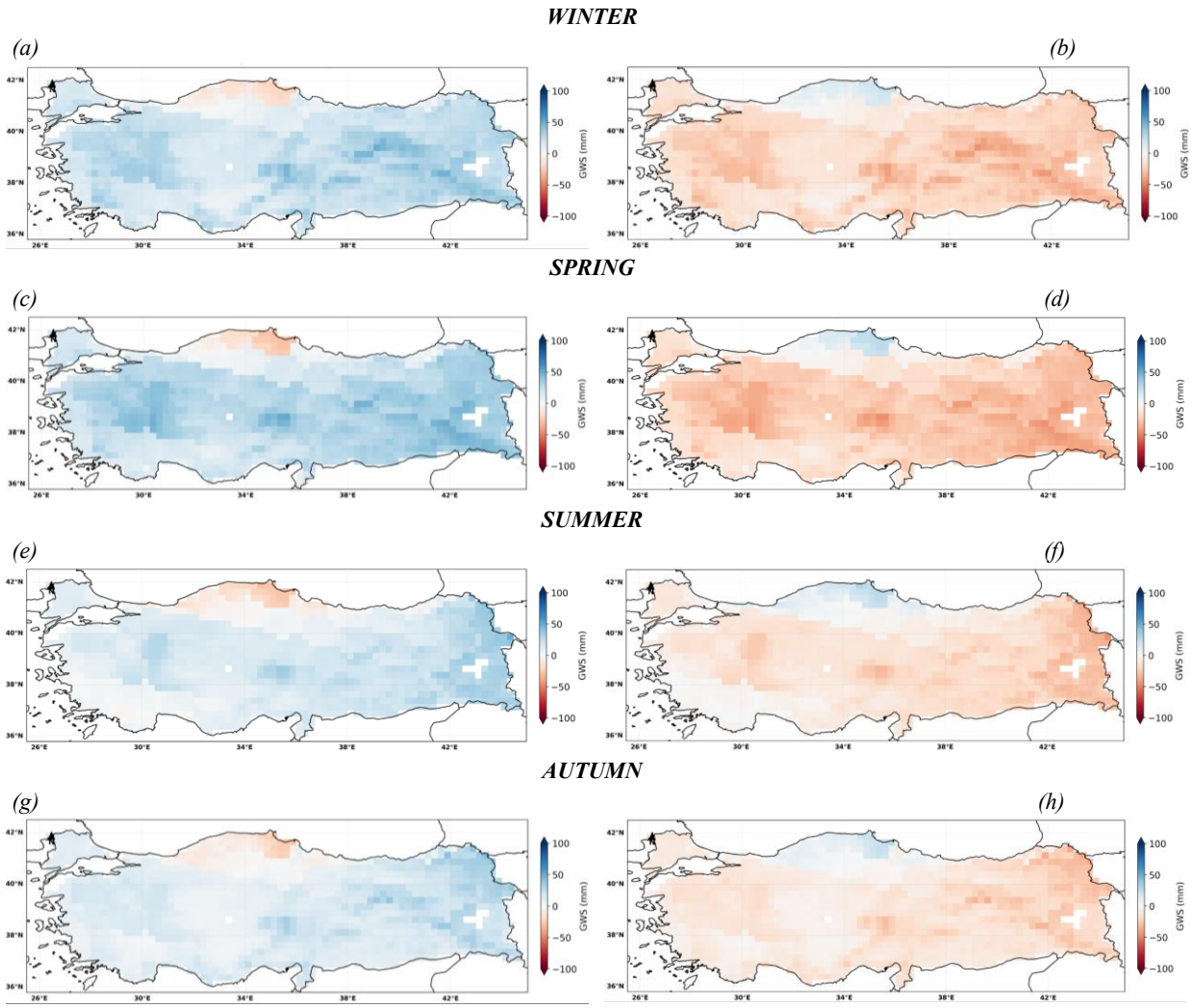

Figure 10. Spatial anomaly distribution of GWS in winter of (a) Period I, (b) Period II; in spring of (c) Period I, (d) Period II; in summer of (e) Period I, (f) Period II; in autumn of (g) Period I, (h) Period II.

3.1.4 Spatial mean analysis based on 21 water years for each watershed

Figure 11 presents the watershed-averaged GWS time series for the 25 main watersheds in Türkiye with their corresponding linear trends. Considerable spatial heterogeneity is evident among the watersheds in both the magnitude and temporal variability of GWS. Most watersheds exhibit negative long-term trends, although the rate of GWS decline varies substantially from one watershed to another. In contrast, only one watershed, the Western Black Sea, displays a slightly increasing trend.

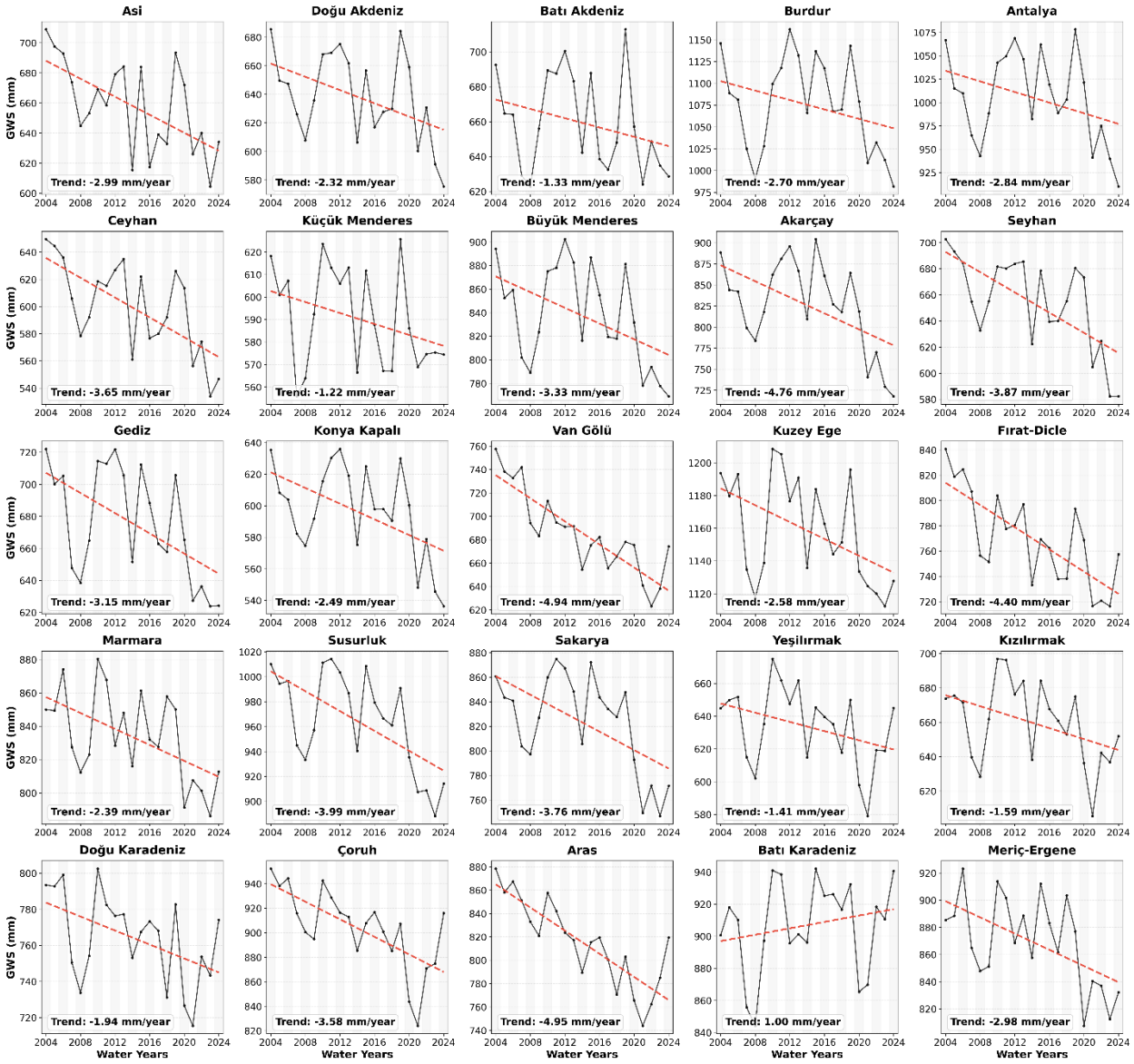

Figure 11. Mean GWS time series and long-term trends for the 25 watersheds.

3.2. Predictive Model

A comprehensive predictive framework based on the GWN architecture has been constructed to model GWS anomalies across the Türkiye. Figure 12 displays the scatter plot of the observed versus predicted GWS anomalies across the independent test period, aggregating the results of all 25 individual watersheds into a unified visualization (comprising a total of 1475 data). In line with standard benchmarking practices in spatiotemporal deep learning, this collective visualization presents the overall generalized performance of the model as an aggregate. The detailed watershed-specific time-series prediction plots for each of the 25 individual watersheds are provided in Figure S4.

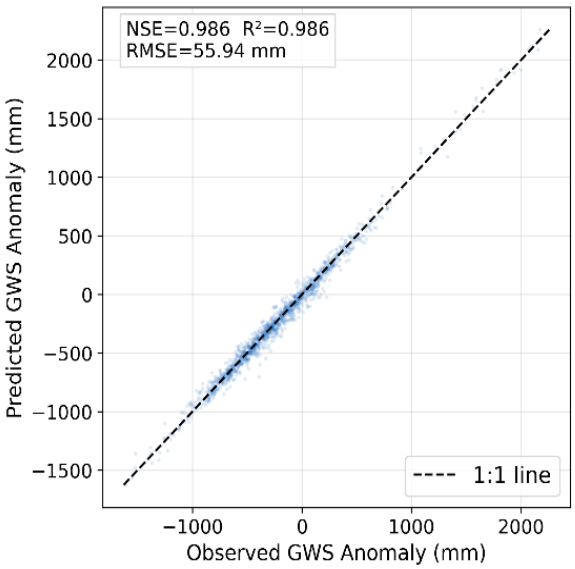

Figure 12. Observed versus predicted GWS anomaly values aggregated across all 25 watersheds and the entire test period (October 2019 – September 2024), yielding NSE = 0.986, R^2 = 0.986, and RMSE = 55.94 mm. Each point represents a monthly prediction for one watershed. The dashed line indicates the 1:1 reference line.

The predictive performance of the GWN model has been evaluated by multiple metrics, including NSE, RMSE, MAPE, and wMAPE. Table 4 presents the overall performance metrics of the 5-year prediction model evaluated individually for each watershed.

Table 4. Performance evaluation metrics of the 5-year GWS anomaly prediction across each individual watershed using GWN.

Watershed	**NSE**	**RMSE**	**MAPE**	**wMAPE**
Akarçay	0.976	29.323	14.33	7.25
Antalya	0.990	45.723	29.99	7.67
Aras	0.931	101.002	46.43	18.76
Asi	0.967	33.872	47.65	14.15
Batı Akdeniz	0.980	57.774	35.71	12.40
Batı Karadeniz	0.964	86.670	49.15	18.4
Burdur	0.961	34.763	17.18	11.81
Büyük Menderes	0.988	42.691	15.66	7.56
Ceyhan	0.987	39.541	23.56	7.81
Doğu Akdeniz	0.993	29.158	20.24	6.16
Doğu Karadeniz	0.976	50.519	71.83	12.65
Fırat-Dicle*	0.993	83.262	18.73	6.38
Gediz	0.986	35.917	24.16	8.49
Konya Kapalı	0.978	54.196	14.18	8.49
Kuzey Ege	0.963	43.707	59.09	14.59
Küçük Menderes	0.975	31.066	26.33	13.45

Kızılırmak	0.987	56.689	21.88	8.24
Marmara	0.983	45.626	24.16	9.15
Meriç-Ergene	0.881	77.563	60.71	20.93
Sakarya	0.981	61.799	46.07	6.06
Seyhan	0.980	49.198	340.17	9.05
Susurluk	0.969	65.848	61.68	10.54
Van Gölü	0.977	37.542	42.51	11.39
Yeşilırmak	0.992	37.951	31.27	7.15
Çoruh	0.942	79.469	135.01	17.31

*Fırat-Dicle is "Tigris-Euphrates" in English.

The fact that the wMAPE values remain below or near 10% across the vast majority of the studied watersheds demonstrates the exceptional predictive accuracy of the model across all individual watersheds. Unlike the standard MAPE, wMAPE delivers far more stable and meaningful evaluations, particularly for datasets like GWS anomalies that frequently contain values near zero.

While the GWN model exhibits high NSE values across all watersheds, indicating strong capture of the overall GWS trend and seasonality, some watersheds show elevated MAPE values. This is attributed to the nature of GWS anomaly, where observed values near zero disproportionately inflate percentage errors even when absolute residuals are minimal. Therefore, the high NSE values are more representative of the model's overall predictive performance in capturing large-scale groundwater dynamics. For instance, in the case of the Seyhan watershed, the model achieved an exceptional NSE of 0.98, visually confirmed by the near-perfect alignment of predicted and observed GWS anomalies during the 60-month independent test period. Closer inspection of the forecasting trajectory reveals that between months 15 and 20, the observed curve (black line) directly touches the zero baseline. Although the standard MAPE reached 340% for this watershed, this figure is identified as a mathematical artifact caused by observed values approaching zero, which disproportionately inflates percentage errors. When evaluated using the wMAPE, which is more robust for anomaly data, the error remains as low as 9.05%.

The high consistency observed across the unseen test dataset indicates that the model has successfully captured the complex spatiotemporal dynamics of the GWS without overfitting. This robust alignment between model predictions and observations strongly validates that the 'feature importances' identified by SHAP reflect true physical realities rather than statistical noise. Consequently, this high predictive accuracy provides a reliable foundation for subsequent XAI analysis via SHAP, ensuring that the identified drivers of GWS variability and the resulting criticality scores are rigorously grounded in high-fidelity model performance.

3.3. Driver attribution with SHAP analysis

In this study, GradientSHAP has been employed to analyze the contribution of GWS, precipitation, ET, and watershed characteristics to the predicted GWS anomaly using the GWN algorithm. The individual SHAP values for each watershed are also provided in Figure S6. Figure 13 illustrates

the percentage contribution of different driver groups to the total SHAP value across all studied watersheds for a 5-year prediction horizon.

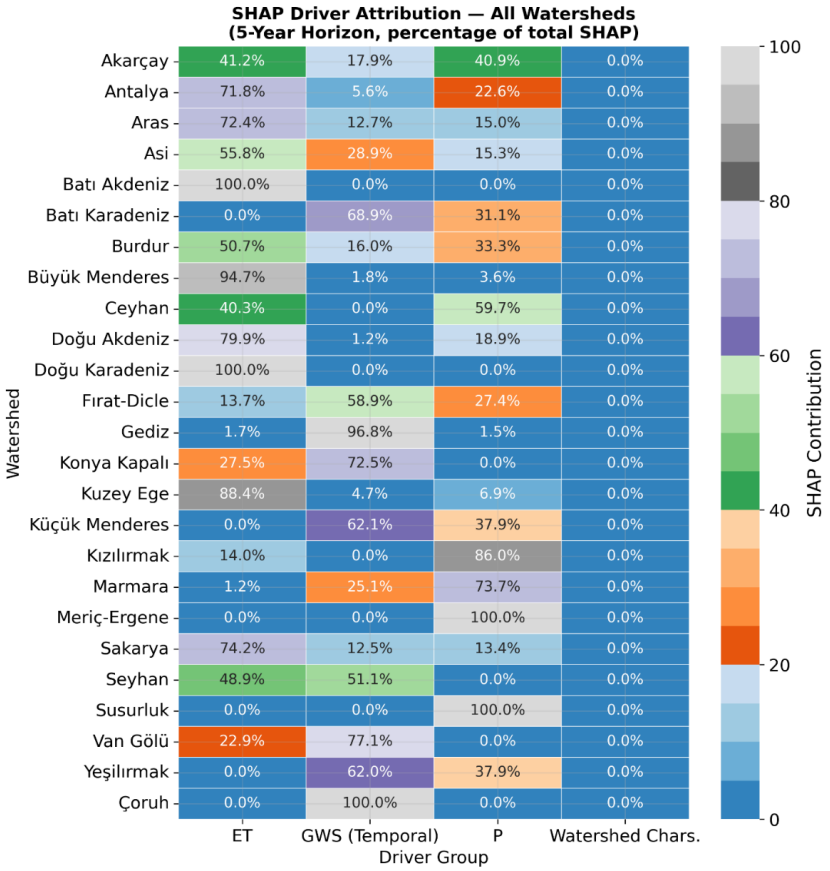

Figure 13. SHAP-based driver attribution across 25 river watersheds for the 5-year forecast horizon. Each cell shows the percentage contribution of a driver group (ET, GWS temporal dynamics, precipitation, and static watershed characteristics) to the total absolute SHAP value for that watershed, summing to 100% across each row. Color intensity indicates the magnitude of SHAP contribution.

According to Figure 16, the SHAP attribution analysis reveals significant spatial variability in driver dominance across the watersheds. For a 5-year horizon, ET emerges as the primary driver in several regions, most notably in Batı Akdeniz and Doğu Karadeniz, where it accounts for 100% of the model's output attribution. Conversely, GWS (temporal) shows a dominant influence in watersheds such as Gediz (96.8%) and Çoruh (100%), indicating that groundwater storage dynamics are the critical factor in these areas. P is the leading driver in Susurluk (100%) and Kızılırmak (86.0%). Interestingly, watershed characteristics show zero contribution across all watersheds for this specific horizon, suggesting that dynamic hydro-climatic variables far outweigh static physical traits in influencing the model's 5-year predictions.

3.4. GWS Criticality assessment and ranking

Figure 14 serves as the primary synthesis of this study's findings, providing a comprehensive criticality ranking of the watersheds.

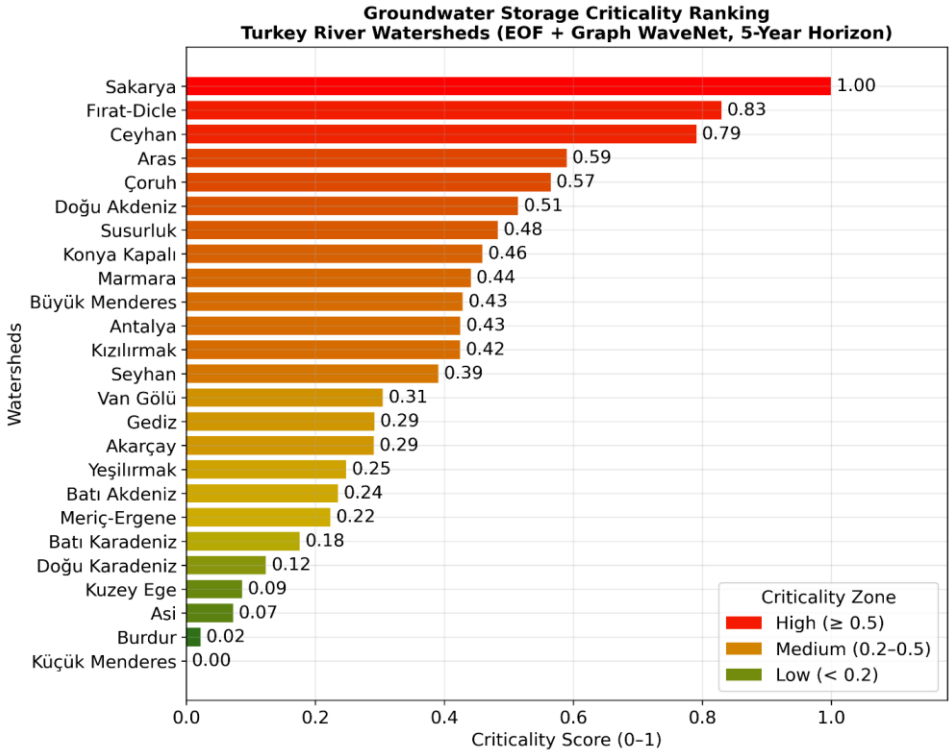

Figure 14. GWS criticality ranking for 25 watersheds, derived from a composite index integrating GWN 5-year predictions, GradientSHAP driver attribution, Mann-Kendall trend analysis, and watershed physical and demographic characteristics. Watersheds are ordered by descending criticality score (0–1). Color zones indicate high (≥0.5, red), medium (0.2–0.5, orange-yellow), and low (<0.2, green) criticality.

According to our results, the Sakarya emerges as the most critical watershed with a normalized score of 1.00. This high criticality can be attributed to several converging factors: (i) a significant declining trend in GWS identified, (ii) high sensitivity to hydro-climatic drivers as revealed by SHAP attribution, and (iii) substantial predicted storage losses over the 5-year horizon, and (iv) elevated population density.

Following Sakarya, the Fırat-Dicle (0.83) and Ceyhan (0.79) watersheds also fall into the very high-criticality zone, signaling an urgent need for targeted groundwater management strategies in these regions. The robustness of this ranking is further validated by sensitivity analyses (Section 3.5), ensuring that the identified priorities remain stable under varying weight perturbations.

3.5 Sensitivity analysis of criticality scores

The individual influence of each index component has been further scrutinized through an OAT sensitivity analysis, as illustrated in Figure 15. In this analysis, each component's weight has varied from 0% to 200% of its baseline value, while others have been rescaled proportionally. As shown in Figure 15a, all sensitivity curves converge at the 100% baseline point (zero rank change). The 'Prediction' component (dark blue line) emerges as the dominant feature, exhibiting the steepest slope and reaching a mean absolute rank change of >3.0 when its weight is eliminated. Conversely, the 'GWS long-term mean' (brown line) and 'GWS minimum' (grey line) show near-zero sensitivity, indicating that these secondary components provide stable but non-volatile contributions to the overall prioritization.

The robustness of the ranking is further confirmed by Kendall's τ correlation analysis in Figure 15b. Across the entire perturbation range, τ remained above the 0.80 threshold for all components, with the sole exception of the 'Prediction' term, which dropped to $\tau \approx 0.6$ only under the extreme scenario of being completely removed (0% weight). This signifies that the overall criticality ranking is highly robust to uncertainties in secondary parameters such as population density or seasonal amplitude. Most importantly, no single component perturbation caused the top-ranked watershed to change across the 0–200% range. This confirms that Sakarya's designation as the most critical region is not an artifact of specific weight assignments but is a fundamental signal driven by the integrated hydro-climatic data.

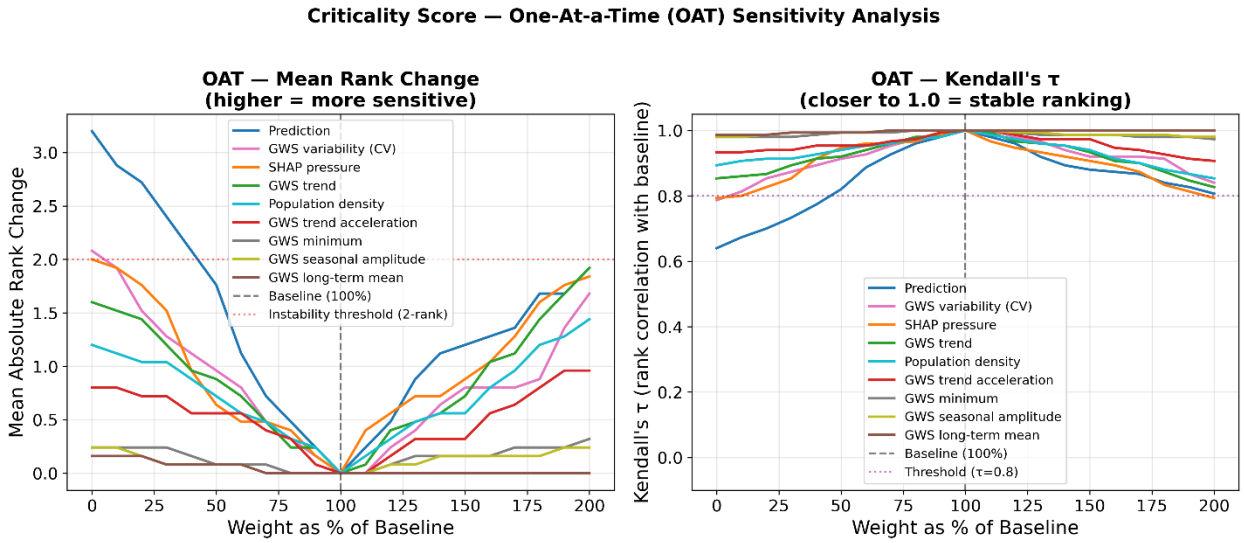

Figure 15. OAT sensitivity analysis. (a) Mean absolute rank change across all 25 watersheds when each component weight varies from 0 to 200% of its assigned value while others are rescaled proportionally. The red dotted line marks the 2-rank instability threshold. (b) Kendall's τ rank correlation between the baseline and perturbed rankings; values approaching 1.0 indicate stable rankings. The green dotted line marks $\tau = 0.80$.

The robustness of the criticality ranking has also been rigorously tested using an MC sensitivity analysis with 10,000 iterations. Figure 16 (a) presents the frequency with which each watershed has been ranked as the most critical across 10000 weighting combinations evaluated in the sensitivity analysis. It demonstrates that the Sakarya, Antalya, and Fırat-Dicle watersheds are consistently identified as the most critical regions, with Sakarya achieving the Rank-1 position in over 30% (≈ 32%) of all simulations regardless of weight perturbations. These three watersheds fall into the 'consistently critical' category (P > 20%), confirming that their high-risk status is a fundamental characteristic of the data rather than an artifact of specific weight assignments. Furthermore, Figure 16 (b) illustrates the rank uncertainty across the 5^{th}-95^{th} percentile range. The narrow uncertainty bands observed for the top-ranked watersheds (Sakarya, Antalya, and Fırat-Dicle) indicate exceptionally high stability in their prioritization. The close alignment between the baseline ranks (red triangles) and the median ranks (black dots) further validates the reliability of the composite index. While some mid-to-low rank watersheds (e.g., Küçük Menderes or Van Gölü) exhibit wider uncertainty intervals, the primary objective of identifying the most urgent intervention zones is achieved with high confidence. These results provide strong evidence that the proposed criticality framework is a dependable tool for regional groundwater management and policy prioritization.

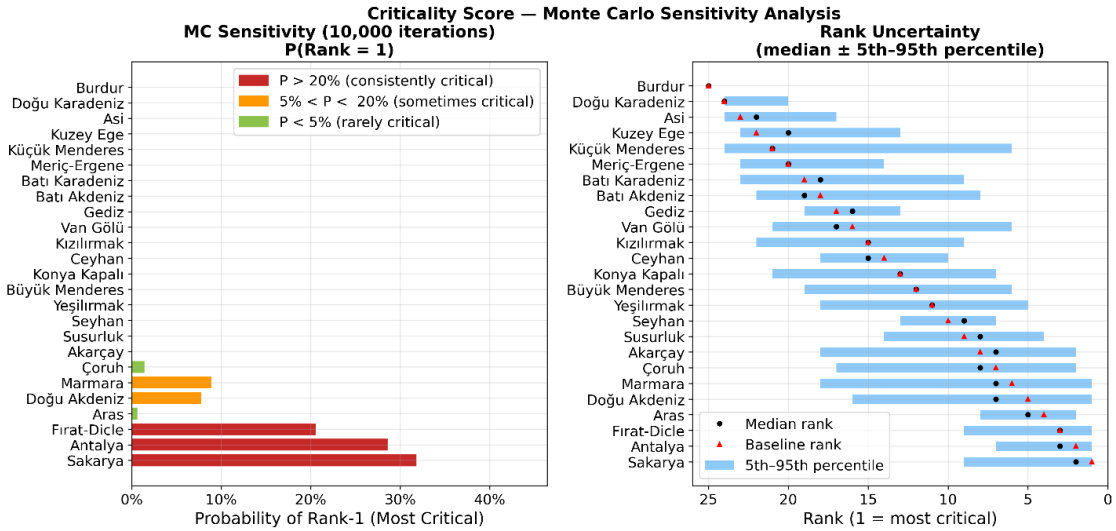

Figure 16. MC sensitivity analysis (n = 10000 iterations) of the criticality ranking. (a) Probability of each watershed achieving Rank-1 (most critical) across randomly sampled weight combinations drawn from a Dirichlet distribution. (b) Rank uncertainty shown as median (•) and 5th–95th percentile range for each watershed; narrow bands indicate stable rankings regardless of weight choice.

Figure 17 shows combined sensitivity analysis results. In Figure 17 (a), the components shown in red (prediction) and orange (GWS variability) exceed the 2-rank instability threshold and are therefore the primary contributors to ranking sensitivity. The SHAP pressure and GWS trend components, also shown in orange, remain close to the threshold, indicating that they also exert a substantial influence on the final ranking. In contrast, the components shown in green (population

density, GWS trend acceleration, GWS minimum, GWS seasonal amplitude, and GWS long-term mean) exhibit relatively low sensitivity and have only a minor effect on the ranking results.

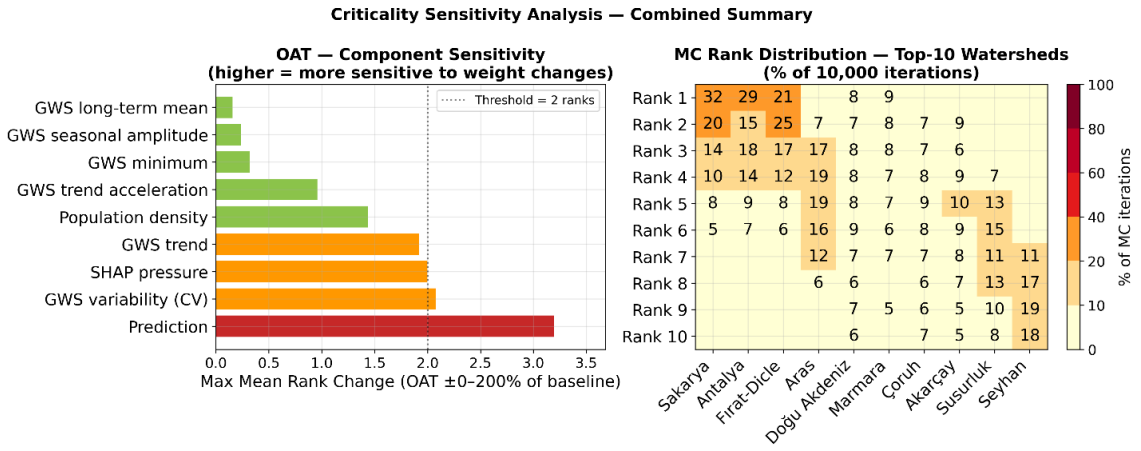

Figure 17. Combined sensitivity analysis results. (a) OAT sensitivity ranking shows the maximum mean rank change when each component weight is varied from 0% to 200% of its assigned value. (b) Heatmap showing MC rank distribution for the top 10 critical watersheds; cell values represent the percentage of 10000 iterations in which each watershed has been assigned the corresponding rank.

The combined results in Figure 17 reconcile the OAT and MC perspectives: the model prediction term is identified as the most influential weighting component (Figure 17(a)), and accordingly, the three watersheds whose criticality is most strongly driven by predictive signal—Sakarya, Antalya, and Fırat-Dicle—together capture 82% of all Rank-1 assignments across the MC simulation (Figure 17(b), top row). Overall, the combined OAT and MC results suggest that the proposed GWS criticality framework is robust to reasonable weight perturbations and that the identified priority watersheds are not artifacts of a single subjective weighting scheme.

4. Conclusion

This study presented an integrated, data-driven framework that combines dimensionality reduction (EOF), spatiotemporal deep learning (e.g., GWN), explainable artificial intelligence (GradientSHAP), and multi-criteria decision analysis to quantify GWS criticality across Türkiye's 25 major watersheds, addressing a pressing need for scalable, physically grounded, and uncertainty-aware tools to support proactive water resource management under intensifying climate and demographic pressures.

The spatial and seasonal analyses revealed a clear and concerning signal: GWS conditions across Türkiye have systematically deteriorated over the past two decades, with the dominance of positive anomalies during 2004–2015 WYs giving way to widespread negative anomalies during 2015–2024 WYs. This shift, observed consistently across all seasons and most pronounced in the central, eastern, and southeastern parts of the study area, indicates that groundwater depletion in Türkiye is no longer confined to isolated drought episodes but reflects a structural, watershed-scale

alteration of the hydrological regime. The substantial heterogeneity observed among watersheds—in trend magnitude, seasonal amplitude, and recovery behavior—further confirms that nationwide or regionally averaged assessments would obscure critical local dynamics, reinforcing the necessity of the watershed-scale modeling approach adopted here.

The GWN architecture has shown strong prediction accuracy across the independent five-year test period (NSE = 0.986, R^2 = 0.986, RMSE = 55.94 mm), successfully capturing both the long-term trajectory and seasonal dynamics of GWS anomalies. This high predictability is not merely a computational gain; it provides the necessary foundation of trust for the subsequent explainability and criticality analyses. Conclusions about driver attribution and watershed vulnerability are only as credible as the model from which they are derived. The GradientSHAP analysis further revealed that the relative influence of precipitation, evapotranspiration, and groundwater memory on predicted GWS varies substantially from one watershed to another, indicating that no single hydro-climatic driver universally governs groundwater behavior across Türkiye and that watershed-specific, rather than generalized, intervention strategies are warranted.

The central contribution of this work is the proposed criticality scoring framework, which moves beyond conventional trend-based assessments by fusing model predictions, SHAP-derived driver confidence, and historical GWS statistics into a single, interpretable index. This approach allows the framework to distinguish between watersheds that may exhibit superficially similar declining trends but differ fundamentally in their underlying drivers, predictive certainty, and resilience capacity, a distinction that purely descriptive trend analyses cannot achieve. Applying this framework identified Sakarya, Antalya, and Fırat-Dicle as the most critical watersheds in Türkiye, driven by a convergence of declining storage trends, high predictive sensitivity to hydro-climatic drivers, and substantial anthropogenic pressure.

Covering approximately 7% of Türkiye's total land area, the Sakarya watershed represents the nation's third-largest watershed and a critical hydrological zone bordering megacity Istanbul and enclosing capital city Ankara. Agricultural activities occupy roughly 50% of the watershed's territory, with irrigation constituting the largest water sector at 74% of total utilization. Driven by rapid demographic growth, expanding urbanization, and intensive groundwater extraction, the region faces severe water stress. Under the Falkenmark indicator, the watershed is also classified as a water-scarce region (Yaykiran et al., 2019; Kayan et al., 2022).

The Antalya watershed exhibits a pronounced vulnerability to hydro-climatic changes, characterized by statistically significant upward trends in both ambient temperatures and open-surface evaporation, alongside a concomitant decline in annual cumulative precipitation. Despite these increasingly arid conditions, expanding agricultural activities have driven a substantial rise in actively irrigated surface areas over time, placing severe stress on the regional water budget. When surface water availability falls short of demanding agricultural requirements, reliance heavily shifts toward groundwater resources. This intensive extraction is further exacerbated by the widespread proliferation of unauthorized and unregulated wells, inducing a chronic depletion of the local aquifer. Consequently, this persistent over-abstraction in heavily cultivated zones has

triggered lateral seawater intrusion along coastal margins, compromising the quality and sustainability of the watershed's vital freshwater resources (Ozcelik, 2022; Karatas et al., 2026).

Fırat-Dicle (Tigris-Euphrates) is a transboundary groundwater resource that originates in the eastern part of Türkiye and flows through Syria to Iraq and Kuwait (Taylor et al., 2013). In this watershed, which is fed by snowmelt, many sectors contributing to the local economy in these countries include hydropower that produces electricity and operates agricultural irrigation systems, recreation, tourism activities (Kibaroglu, 2019), and supporting wildlife (Biricik et al., 2024). Hydroclimatic drivers and drought conditions are of great importance in groundwater depletion in this basin (Abdelmohsen et al., 2022; Chao et al., 2018)

Critically, the reliability of this prioritization has not been assumed but rigorously tested. Through complementary OAT and MC sensitivity analyses involving 10000 simulated weighting scenarios, this study demonstrated that the identification of Sakarya, Antalya, and Fırat-Dicle as the most urgent intervention zones are a robust feature of the underlying data, rather than an artifact of subjective weight selection; these three watersheds collectively captured the top rank in over 80% of all simulations. This sensitivity-validated robustness is, to our knowledge, rarely demonstrated in comparable groundwater criticality studies and represents a methodological contribution that strengthens the defensibility of the framework for operational decision-making.

While Sakarya, Fırat-Dicle, and Ceyhan represent the highest baseline criticality scores, a broader synthesis across the sensitivity-tested ranking (Figures 14–17) and watershed demographic characteristics identifies ten watersheds warranting sustained monitoring and prioritized intervention: Sakarya, Antalya, Fırat-Dicle, Ceyhan, Aras, Marmara, Çoruh, Susurluk, Doğu Akdeniz, and Konya Kapalı. Notably, Antalya did not rank among the top three in the baseline composite score yet emerged as the second most consistently critical watershed in the MC sensitivity analysis (P(Rank-1) ≈ 28%), underscoring the value of sensitivity-based validation in surfacing watersheds whose criticality may otherwise be underestimated by a single weighting scheme. Similarly, Marmara, despite a moderate hydrological trend, carries disproportionate significance due to its exceptionally high population density (approximately 10.6 million inhabitants concentrated within one of the smallest watershed areas in the country), illustrating that demographic pressure can elevate a watershed's practical urgency independently of its purely hydrological signal. Konya Kapalı, as an endorheic (closed) basin lacking natural outflow, exhibits structural vulnerability to storage depletion that merits continued attention despite wider rank uncertainty in the sensitivity analysis. Collectively, this expanded set of ten watersheds reflects the convergence of three independent lines of evidence, baseline criticality scoring, sensitivity-based rank robustness, and demographic exposure, and is recommended as the primary focus for near-term groundwater monitoring and management interventions in Türkiye. Table 5 indicates top 10 critical watersheds in Türkiye.

Table 5. Top 10 critical watersheds in Türkiye identified through baseline composite criticality scoring (Figure 11), sensitivity-based rank robustness (Figures 12-14), and watershed demographic exposure.

Rank	Watershed	Baseline Score	MC P (Rank-1)*	Evidence Tier	Rationale	Classification Rationale
1	Sakarya	1.00	32%	Consistently critical	Highest baseline composite score; most stable Rank-1 watershed; strong declining trend; urban-industrial demand; water pollution; compounded by high population density. In addition, the Melen Project, megacity Istanbul's primary water supply lifeline, depends on critical infrastructure traversing this watershed.	Collectively account for 82% of all Rank-1 assignments across 10000 MC iterations. These watersheds consistently emerge as critical, demonstrating high stability regardless of weight perturbations.
2	Antalya	0.43	28%	Consistently critical	Karstic travertine aquifer under dual pressure from rapid tourism growth and intensive greenhouse agriculture; significant aquifer depletion driven by excessive borehole extraction on the travertine plateau, exacerbated by intensifying climatic stress.	
3	Fırat-Dicle	0.83	21%	Consistently critical	High geopolitical vulnerability as a major transboundary watershed; second-highest baseline criticality score; strong declining trend; natural flow regimes are significantly altered by extensive GAP project infrastructure (>20 dams).	
4	Ceyhan	0.79	-	High composite criticality	Third-highest baseline criticality score; strong declining trend; characterized by dense agricultural irrigation and water pollution, with high vulnerability to	Primarily identified by baseline composite scores; these watersheds exhibit moderate stability under weight perturbation,

					Mediterranean climate variability.	indicating a consistent yet more sensitive criticality.
5	Aras	0.59	1%	High composite criticality	Geopolitical vulnerability as a transboundary watershed; exhibits a strong declining trend and increased sensitivity to climate-driven shifts in runoff timing.	
6	Marmara	0.44	9%	Emerging risk	Intense demographic pressure (~19 million inhabitants) concentrated within a limited area, leading to significant industrial and domestic water scarcity and pollution risks.	Criticality evidence extends beyond baseline scoring, incorporating sensitivity rank robustness and high demographic exposure as primary drivers for continued monitoring.
7	Çoruh	0.57	2%	Emerging risk	Strong declining trend; characterized by steep topography and extensive hydroelectric infrastructure; consistently identified as a top-10 critical watershed in MC simulations.	
8	Susurluk	0.48	-	Emerging risk	Dense agricultural and industrial use; strong declining trend; recurrent presence in the MC top-10 heatmap; water quality is compromised by a combination of agricultural runoff, industrial waste, and natural boron deposits; moderate-to-high population density.	
9	Doğu Akdeniz	0.51	8%	Emerging risk	High exposure to coastal erosion and sea level rise, increasing the risk of saltwater intrusion into freshwater resources.	

10	Konya Kapalı	0.46	-	Emerging risk	Endorheic (closed) watershed lacking natural outflow; watershed with the least rainfall; dense agricultural use; vulnerability is driven by intensive irrigation and extreme drought, leading to over-extraction and sinkhole formation. Current water-intensive crop patterns are increasingly unsustainable.	

*MC P(Rank = 1): probability of each watershed achieving the top rank (Rank = 1) across 10000 MC weight perturbation iterations drawn from a Dirichlet distribution.

Beyond its application to Türkiye, the proposed framework offers a transferable blueprint for groundwater risk assessment in other data-scarce or hydrologically heterogeneous regions, particularly where satellite-derived storage estimates, climatic forcing data, and basic demographic information are available. Future work should extend this framework by incorporating direct groundwater abstraction data where available, exploring ensemble or probabilistic forecasting to quantify predictive uncertainty alongside point estimates, and evaluating the framework's performance under future climate projection scenarios to anticipate, rather than merely diagnose, emerging groundwater stress. As Türkiye's population continues to grow and climate variability intensifies, frameworks such as the one presented here, capable of identifying not only where groundwater systems are declining but also why and with what degree of confidence, will be indispensable for translating hydrological monitoring into actionable, defensible water policy.

Data Availability

All data used in this study is publicly available. GWS data can be found in https://disc.gsfc.nasa.gov/datasets/GLDAS_CLSM025_DA1_D_2.2/summary. ECMWF's ERA5-land hourly precipitation and AgERA5 potential evapotranspiration data can be found in https://doi.org/10.24381/cds.e2161bac and https://doi.org/10.24381/f9c1f09d, respectively. The number of district-level populations can be obtained through https://veriportali.tuik.gov.tr/en/databrowser/tuik/categories/11/11_1/11_1_1/TR,DF_ADNKS_T22,1.1.

References

Abdelmohsen, K., Sultan, M., Save, H., Abotalib, A. Z., Yan, E., & Zahran, K. H. (2022). Buffering the impacts of extreme climate variability in the highly engineered Tigris Euphrates river system. *Scientific Reports*, *12*(1), 4178. https://doi.org/10.1038/s41598-022-07891-0

Adam, M. A., Scheiber-Enslin, S. E., & Ali, K. A. (2026). Application of random forest modeling to evaluate groundwater storage changes in the Breede Water Management Area, South Africa. *Hydrogeology Journal*, 1-16. https://doi.org/10.1007/s10040-026-03047-w

Aeschbach-Hertig, W., & Gleeson, T. (2012). Regional strategies for the accelerating global problem of groundwater depletion. *Nature Geoscience*, *5*(12), 853-861. https://doi.org/10.1038/ngeo1617

Ahmadi, H., Kaya, O. A., Babadagi, E., Savas, T., & Pekkan, E. (2020). GIS-based groundwater potentiality mapping using AHP and FR models in central Antalya, Turkey. *Environmental Sciences Proceedings*, *5*(1), 11. https://doi.org/10.3390/IECG2020-08741

Aksoy, N., Şimşek, C., & Gunduz, O. (2009). Groundwater contamination mechanism in a geothermal field: a case study of Balcova, Turkey. *Journal of contaminant hydrology*, *103*(1-2), 13-28. https://doi.org/10.1016/j.jconhyd.2008.08.006

Baba, A., & Tayfur, G. (2011). Groundwater contamination and its effect on health in Turkey. *Environmental Monitoring and Assessment*, *183*(1), 77-94. https://doi.org/10.1007/s10661-011-1907-z

Baydaroğlu, Ö., & Demir, I. (2024). Temporal and spatial satellite data augmentation for deep learning-based rainfall nowcasting. *Journal of Hydroinformatics*, *26*(3), 589-607. https://doi.org/10.2166/hydro.2024.235

Baydaroğlu, Ö., Muste, M., Cikmaz, A. B., Kim, K., Meselhe, E., & Demir, I. (2024). Testing protocols for smoothing datasets of hydraulic variables acquired during unsteady flows. *Hydrological Sciences Journal*, *69*(13), 1813-1830. https://doi.org/10.1080/02626667.2024.2394169

Baydaroğlu, Ö., Yeşilköy, S., Dave, A., Linderman, M., & Demir, I. (2025). Modeling Algal Toxin Dynamics and Integrated Web Framework for Lakes. *Toxins*, *17*(7), 338. https://doi.org/10.3390/toxins17070338

Biricik, M., Safi, K., & Turğa, Ş. (2024). Remote Sensing Data Reveal a Significant Reduction in the Area of the Nesting Habitat of Rafetus euphraticus in the Tigris River, Southeastern Turkey. *Ecology and Evolution*, *14*(12), e70691. https://doi.org/10.1002/ece3.70691

Bozdağ, A., Ünal, Z., Karkınlı, A. E., Soomro, A. B., Mir, M. S., & Gulzar, Y. (2025). An Integrated Approach for Groundwater Potential Prediction Using Multi-Criteria and Heuristic Methods. *Water*, *17*(8), 1212. https://doi.org/10.3390/w17081212

Campelo, F., Batista, L. S., Takahashi, R. H., Diniz, H. E., & Carrano, E. G. (2016). Multicriteria transformer asset management with maintenance and planning perspectives. *IET Generation, Transmission & Distribution*, *10*(9), 2087-2097. https://doi.org/10.1049/iet-gtd.2015.1112

Castillo, J. N., Resabala, V. F., Freire, L. O., & Corrales, B. P. (2022). Modeling and sensitivity analysis of the building energy consumption using the Monte Carlo method. *Energy Reports*, *8*, 518-524. https://doi.org/10.1016/j.egyr.2022.10.198

Chakraborty, D., Başağaoğlu, H., Gutierrez, L., & Mirchi, A. (2021). Explainable AI reveals new hydroclimatic insights for ecosystem-centric groundwater management. *Environmental Research Letters*, *16*(11), 114024. https://doi.org/10.1088/1748-9326/ac2fde

Chao, N., Luo, Z., Wang, Z., & Jin, T. (2018). Retrieving groundwater depletion and drought in the Tigris-Euphrates Basin between 2003 and 2015. *Groundwater*, *56*(5), 770-782. https://doi.org/10.1111/gwat.12611

Chihana, S., Mbale, J., & Chaamwe, N. (2026). BREATHE: Interpretable Stacked Hybrid Models for Multi-Disease Prediction of SO 2-Linked Respiratory Illnesses in Kankoyo, a Mining Community in Zambia. *IEEE Access*. https://doi.org/10.1109/ACCESS.2026.3670712

Clark, S. R., Fu, G., & Janardhanan, S. (2025). Explainable AI for interpreting spatiotemporal groundwater predictions. *Water Resources Research*, *61*(10), e2025WR041303. https://doi.org/10.1029/2025WR041303

Conlin, M. P., Adams, P. N., Jaeger, J. M., & MacKenzie, R. (2020). Quantifying seasonal-to-interannual-scale storm impacts on morphology along a cuspate coast with a hybrid empirical orthogonal function approach. *Journal of Geophysical Research: Earth Surface*, *125*(12), e2020JF005617. https://doi.org/10.1029/2020JF005617

Davari, S., Eslamian, S., Jamali, M., & Safavi, H. R. (2025). Application of machine learning algorithms for groundwater level prediction in the Najafabad plain. *Scientific Reports, 16,* 2476. https://doi.org/10.1038/s41598-025-32376-1

Davraz, A., & Batur, B. (2021). Hydrogeochemistry characteristics of groundwater and health risk assessment in Yalvaç–Gelendost basin (Turkey). *Applied Water Science*, *11*(4), 67. https://doi.org/10.1007/s13201-021-01401-9

Demiray, B. Z., Mermer, O., Baydaroğlu, Ö., & Demir, I. (2025). Predicting harmful algal blooms using explainable deep learning models: A comparative study. *Water*, *17*(5), 676. https://doi.org/10.3390/w17050676

Demirci, M., Üneş, F., & Körlü, S. (2019). Modeling of groundwater level using artificial intelligence techniques: a case study of Reyhanli region in Turkey. *Applied Ecology & Environmental Research*, *17*(2). http://dx.doi.org/10.15666/aeer/1702_26512663

Dilcan, C. C., & Koksal, M. A. (2026). Basin-based evaluation of the water–energy–climate nexus in Türkiye: Climate scenarios-based ANFIS and GIS assessment. *Journal of Hydrology: Regional Studies*, *65*, 103477. https://doi.org/10.1016/j.ejrh.2026.103477

Di Lullo, G., Gemechu, E., Oni, A. O., & Kumar, A. (2020). Extending sensitivity analysis using regression to effectively disseminate life cycle assessment results. *The International Journal of Life Cycle Assessment*, *25*(2), 222-239. https://doi.org/10.1007/s11367-019-01674-y

Djessou, R. D., Wan, X., Yi, S., Annan, R. F., Su, X., & Wang, S. (2022). Water storage variation and its possible causes detected by GRACE in the Volta River Basin. *Remote Sensing*, *14*(21), 5319. https://doi.org/10.3390/rs14215319

Ertürk, A., Ekdal, A., Gürel, M., Karakaya, N., Guzel, C., & Gönenç, E. (2014). Evaluating the impact of climate change on groundwater resources in a small Mediterranean watershed. *Science of the total environment*, *499*, 437-447. https://doi.org/10.1016/j.scitotenv.2014.07.001

Fraehr, N., Wang, Q. J., Wu, W., & Nathan, R. (2022). Upskilling low-fidelity hydrodynamic models of flood inundation through spatial analysis and Gaussian process learning. *Water Resources Research*, *58*(8), e2022WR032248. https://doi.org/10.1029/2022WR032248

Gardner, M. W., & Dorling, S. R. (1998). Artificial neural networks (the multilayer perceptron)—a review of applications in the atmospheric sciences. *Atmospheric environment*, *32*(14-15), 2627-2636. https://doi.org/10.1016/S1352-2310(97)00447-0

Ge, H., & Asgarpoor, S. (2011). Parallel Monte Carlo simulation for reliability and cost evaluation of equipment and systems. *Electric power systems research*, *81*(2), 347-356. https://doi.org/10.1016/j.epsr.2010.09.012

Gleeson, T., Wada, Y., Bierkens, M. F., & Van Beek, L. P. (2012). Water balance of global aquifers revealed by groundwater footprint. *Nature*, *488*(7410), 197-200. https://doi.org/10.1038/nature11295

Ghosh, A., Pinki, F. T., Baidya, R., Alam, F., & Mandal, S. (2026, April). A Machine Learning and DEM-Based Approach for Predicting Sea Level Rise and Assessing Coastal Risk in Bangladesh Using AI Insights. In *2026 IEEE 15th International Conference on Communication Systems and Network Technologies (CSNT)* (pp. 199-204). IEEE. https://doi.org/10.1109/CSNT69054.2026.11502358

Güler, C., Kurt, M. A., Alpaslan, M., & Akbulut, C. (2012). Assessment of the impact of anthropogenic activities on the groundwater hydrology and chemistry in Tarsus coastal plain (Mersin, SE Turkey) using fuzzy clustering, multivariate statistics and GIS techniques. *Journal of Hydrology*, *414*, 435-451. https://doi.org/10.1016/j.jhydrol.2011.11.021

Gunduz, O., Simsek, C., & Hasozbek, A. (2010). Arsenic pollution in the groundwater of Simav Plain, Turkey: its impact on water quality and human health. *Water, air, and soil pollution*, *205*(1), 43-62. https://doi.org/10.1007/s11270-009-0055-3

Ham, Y. G., Kim, J. H., & Luo, J. J. (2019). Deep learning for multi-year ENSO forecasts. *Nature*, *573*(7775), 568-572. https://doi.org/10.1038/s41586-019-1559-7

Hannachi, A., Jolliffe, I. T., & Stephenson, D. B. (2007). Empirical orthogonal functions and related techniques in atmospheric science: A review. *International journal of climatology*, *27*(9), 1119-1152. https://doi.org/10.1002/joc.1499

Helton, J. C. (1993). Uncertainty and sensitivity analysis techniques for use in performance assessment for radioactive waste disposal. *Reliability Engineering & System Safety*, *42*(2-3), 327-367. https://doi.org/10.1016/0951-8320(93)90097-I

Kara, H. (2025). The prediction of heavy metal contamination in groundwater using machine learning algorithms: a case study from the Harran Plain, a major agricultural irrigation area in Türkiye. *Environmental Geochemistry and Health*, *47*(8), 328. https://doi.org/10.1007/s10653-025-02644-0

Karatas, B. S., Cetinkaya, B., & Cengil, B. (2026). Spatial and temporal trend analysis of groundwater depth and salinity using geostatistics integrated with GIS in the Koprucay irrigation system in Antalya, Turkey. *Irrigation and Drainage*, *75*(1), 290-304. https://doi.org/10.1002/ird.70031

Kavurmaci, M., & Üstün, A. K. (2016). Assessment of groundwater quality using DEA and AHP: a case study in the Sereflikochisar region in Turkey. *Environmental monitoring and assessment*, *188*(4), 258. https://doi.org/10.1007/s10661-016-5259-6

Kayan, G., Türker, U., & Erten, E. (2022). Uncertainty quantification of multi-source hydrological data products for the improvement of water budget estimations in small-scale Sakarya basin, Turkey. *Hydrological Sciences Journal*, *67*(10), 1609-1622. https://doi.org/10.1080/02626667.2022.2093642

Kibaroglu, A. (2019). State-of-the-art review of transboundary water governance in the Euphrates–Tigris river basin. *International Journal of Water Resources Development*, *35*(1), 4-29. https://doi.org/10.1080/07900627.2017.1408458

Kuang, X., Liu, J., Scanlon, B. R., Jiao, J. J., Jasechko, S., Lancia, M., ... & Zheng, C. (2024). The changing nature of groundwater in the global water cycle. *Science*, *383*(6686), eadf0630. https://doi.org/10.1126/science.adf0630

Li, B., H. Beaudoing, and M. Rodell, NASA/GSFC/HSL (2020), GLDAS Catchment Land Surface Model L4 daily 0.25 x 0.25 degree GRACE-DA1 V2.2, Greenbelt, Maryland, USA, Goddard Earth Sciences Data and Information Services Center (GES DISC), Accessed: [*Last Accessed on June 29, 2026*], 10.5067/TXBMLX370XX8

Li, W., Bao, L., Yao, G., Wang, F., Guo, Q., Zhu, J., ... & Lu, S. (2024). The analysis on groundwater storage variations from GRACE/GRACE-FO in recent 20 years driven by influencing factors and prediction in Shandong Province, China. *Scientific Reports*, *14*(1), 5819. https://doi.org/10.1038/s41598-024-55588-3

Li, S., Liu, P., Chen, J., Li, X., & Hua, R. (2026). Energy-efficient adaptive sampling for IIoT via deep perception and reinforcement learning. *Journal of King Saud University Computer and Information Sciences*. https://doi.org/10.1007/s44443-026-00836-x

Lorenz, E. N. (1956). *Empirical orthogonal functions and statistical weather prediction* (Vol. 1, p. 52). Cambridge: Massachusetts Institute of Technology, Department of Meteorology.

Lundberg, S. M., & Lee, S. I. (2017). A Unified Approach to Interpreting Model Predictions. *NeurIPS*.

Lundberg, S. M., & Lee, S. I. (2017). A unified approach to interpreting model predictions. *Advances in neural information processing systems*, *30*.

Lundberg, S. M., Erion, G., Chen, H., DeGrave, A., Prutkin, J. M., Nair, B., ... & Lee, S. I. (2020). From local explanations to global understanding with explainable AI for trees. *Nature machine intelligence*, *2*(1), 56-67. https://doi.org/10.1038/s42256-019-0138-9

Mermer, O., Liu, Y., Jennissen, C. A., Sonka, M., & Demir, I. (2026). Agricultural Injury Severity Prediction Using Integrated Data-Driven Analysis: Global Versus Local Explainability Using SHAP. *Safety*, *12*(1), 6. https://doi.org/10.3390/safety12010006

Morris, M. D. (1991). Factorial sampling plans for preliminary computational experiments. *Technometrics*, *33*(2), 161-174.

Nas, B., & Berktay, A. (2006). Groundwater contamination by nitrates in the city of Konya,(Turkey): A GIS perspective. *Journal of Environmental management*, *79*(1), 30-37. https://doi.org/10.1016/j.jenvman.2005.05.010

Owais, M., & Ramadan, I. (2025). Integrated Deep Learning and Global Sensitivity Analysis Framework for Transportation Link Criticality Evaluation. *Transportation Research Record*, 03611981251394975. https://doi.org/10.1177/03611981251394975

Ozdemir, A. (2011). Using a binary logistic regression method and GIS for evaluating and mapping the groundwater spring potential in the Sultan Mountains (Aksehir, Turkey). *Journal of Hydrology*, *405*(1-2), 123-136. https://doi.org/10.1016/j.jhydrol.2011.05.015

Ozcelik, M. (2022). Potential effects of excessive water withdrawal from boreholes drilled in the Antalya (Turkey) travertine plateau and well interactions. *Euro-Mediterranean Journal for Environmental Integration*, *7*(2), 241-249. https://doi.org/10.1007/s41207-022-00314-6

Raju, A., Singh, R. P., & Sinha, M. (2024, July). Predicting Change in Groundwater Storage Associated to Hydroclimatic Variability in the Indo-Gangetic Plains, India. In *IGARSS 2024-2024 IEEE International Geoscience and Remote Sensing Symposium* (pp. 389-392). IEEE. https://doi.org/10.1109/IGARSS53475.2024.10641842

Rathore, N., Rathore, P., Basak, A., Nistala, S. H., & Runkana, V. (2021, December). Multi scale graph wavenet for wind speed forecasting. In *2021 IEEE International Conference on Big Data (Big Data)* (pp. 4047-4053). IEEE. https://doi.org/10.1109/BigData52589.2021.9671624

Salih, A. M., Raisi-Estabragh, Z., Galazzo, I. B., Radeva, P., Petersen, S. E., Lekadir, K., & Menegaz, G. (2025). A perspective on explainable artificial intelligence methods: SHAP and LIME. *Advanced Intelligent Systems*, *7*(1), 2400304. https://doi.org/10.1002/aisy.202400304

Shapley, L. S. (1953). A value for n-person games. Contributions to the Theory of Games, 2(28), 307-317.

Singh, A. R., Agarwal, A. B., & Singh, D. B. (2022). Sensitivity analysis of double slope solar still having compound parabolic concentrator integrated ETCs by incorporating heat transfer

coefficients, exergy gain and exergy efficiency. *Desalination and Water Treatment*, *276*, 13-27. https://doi.org/10.5004/dwt.2022.28897

Taşan, M. (2025). Improved prediction of groundwater quality index by hybrid machine learning models in a coastal region: A case study from Southern Turkey. *International Journal of Environmental Research*, *19*(4), 147. https://doi.org/10.1007/s41742-025-00814-7

Tayfur, G., Kirer, T., & Baba, A. (2008). Groundwater quality and hydrogeochemical properties of Torbalı Region, Izmir, Turkey. *Environmental Monitoring and Assessment*, *146*(1), 157-169. ttps://doi.org/10.1007/s10661-007-0068-6

Taylor, R. G., Scanlon, B., Döll, P., Rodell, M., Van Beek, R., Wada, Y., ... & Treidel, H. (2013). Ground water and climate change. *Nature climate change*, *3*(4), 322-329. https://doi.org/10.1038/nclimate1744

Tokatli, C., Köse, E., & Çiçek, A. (2013). Groundwater Quality of Türkmen Mountain, Turkey. *Polish Journal of Environmental Studies*, *22*(4).

Türkiye Su Enstitüsü (SUEN). Havza Yönetim Planları Verileri.

Usta, A. (2016). Türkiye'nin Su Potansiyelinin Belirlenmesi Üzerine Bir Araştirma. *Küresel Mühendislik Çalışmaları Dergisi*, *3*(2), 107-115. https://izlik.org/JA54YL33CZ

Wang, B., Lee, J. Y., & Xiang, B. (2015). Asian summer monsoon rainfall predictability: a predictable mode analysis. *Climate Dynamics*, *44*(1), 61-74. https://doi.org/10.1007/s00382-014-2218-1

Wu, Z., Pan, S., Long, G., Jiang, J., & Zhang, C. (2019). Graph wavenet for deep spatial-temporal graph modeling. *arXiv preprint arXiv:1906.00121*. https://doi.org/10.48550/arXiv.1906.00121

Yaykiran, S., Cuceloglu, G., & Ekdal, A. (2019). Estimation of water budget components of the Sakarya River Basin by using the WEAP-PGM model. *Water*, *11*(2), 271. https://doi.org/10.3390/w11020271

Yazicigil, H., & Ekmekci, M. (2019). Groundwater. In *Water Resources of Turkey* (pp. 159-201). Cham: Springer International Publishing. https://doi.org/10.1007/978-3-030-11729-0_6

Yesilnacar, M. I., Sahinkaya, E., Naz, M., & Ozkaya, B. (2008). Neural network prediction of nitrate in groundwater of Harran Plain, Turkey. *Environmental Geology*, *56*(1), 19-25. https://doi.org/10.1007/s00254-007-1136-5

Yetiş, R., Atasoy, A. D., Demir Yetiş, A., & Yeşilnacar, M. İ. (2019). Hydrogeochemical characteristics and quality assessment of groundwater in Balikligol Basin, Sanliurfa, Turkey. *Environmental Earth Sciences*, *78*(11), 331. https://doi.org/10.1007/s12665-019-8330-0

Yeşilköy, S., Baydaroğlu, Ö., Singh, N., Sermet, Y., & Demir, I. (2024). A contemporary systematic review of cyberinfrastructure systems and applications for flood and drought data analytics and communication. *Environmental Research Communications*, *6*, 102003. https://doi.org/10.1088/2515-7620/ad85c4

Yeşilköy, S., & Baydaroğlu, Ö. (2025). Rain-on-snow climatology and its impact on flood risk in snow-dominated regions of Türkiye. *Theoretical and Applied Climatology*, *156*, 239. https://doi.org/10.1007/s00704-025-05463-6

Zhang, Z. (2018, June). Improved adam optimizer for deep neural networks. In *2018 IEEE/ACM 26th international symposium on quality of service (IWQoS)* (pp. 1-2). IEEE. https://doi.org/10.1109/IWQoS.2018.8624183